universität wien

MASTERARBEIT / MASTER'S THESIS

Titel der Masterarbeit / Title of the Master's Thesis

„Ferroelectric phase transition: A DFT study of soft phonon modes in KTaO3 “

verfasst von / submitted by

Josef Huber BSc

angestrebter akademischer Grad / in partial fulfilment of the requirements for the degree of

Master of Science (MSc)

Wien, 2022 / Vienna, 2022

Studienkennzahl lt. Studienblatt / degree programme code as it appears on the student record sheet:	A 066 876
Studienrichtung lt. Studienblatt / degree programme as it appears on the student record sheet:	Physik
Betreut von / Supervisor:	Univ.-Prof. Dr.techn. Cesare Franchini
Mitbetreut von / Co-Supervisor:	Dr. Michele Reticcioli

Abstract

Ferroelectric materials enable the switch of internal dipole moments by applying an external electric field. They attract great attention in solid-state physics and allow for a large variety of technological applications in modern devices such as capacitors, non-volatile memories or light detectors.

Perovskite oxides are ionic materials that might undergo ferroelectric phase transitions. More problematic is the $KTaO_3$ perovskite that is mostly referred as a quantum paraelectric, where ferroelectricity is suppressed by quantum fluctuations. It is not entire clear whether the material undergoes a ferroelectric phase transition under certain conditions, such as applied isotropic pressure.

With the advent of computers, the study of materials in the framework of density functional theory (DFT) has greatly improved solid-state physics by confirming experiments and predicting physical properties of a great variety of materials. The so called soft-mode theory of phonons provide a convenient method to study ferroelectric phase transitions using DFT. Within this model, an indication of a phase instability is revealed by the vanishing frequency of a phonon mode, which can become also negative.

In this work I present a detailed investigation of electronic, structural and vibrational properties of $KTaO_3$ using different approaches within DFT. Phonon modes are calculated, first under change of isotropic pressure and secondly by correcting the electronic correlation which is poorly captured in standard DFT. Under various conditions soft phonon modes are found, indicating a phase transition. This approach led to the identification of soft phonon modes and phase instabilities, under various conditions of applied pressure. Finally, by condensing the unstable phonons, I obtained the structural transition to the corresponding lower symmetry phases. The ferroelectric structures obtained with this methodology show small energy difference with the paraelectric crystal, supporting the quantum paraelectric model for $KTaO_3$.

Zusammenfassung

Ferroelektrische Materialien sind dadurch definiert, dass ihre internen Dipolmomente durch Anlegen eines elektrischen Feldes polarisiert werden. Ihre Wichtigkeit in der Festkörperphysik hebt sich durch diverse technische Anwendungen, wie Kondensatoren, nichtflüchtigen Speicher oder Lichtdetektoren hervor.

Perovskite sind ionische Materialien, die unter Umständen ferroelektrisch sind. Im Falle des Perovskiten $KTaO_3$ wird die Ferroelektrizität jedoch durch Quantenfluktuationen unterdrückt und wird daher als quantenparaelektrisch bezeichnet. Es ist jedoch nicht vollständig geklärt, ob ein ferroelektrischer Phasenübergang unter gewissen Umständen wie etwa äußerem isotropen Druck möglich ist.

Die Dichtefunktionaltheorie (DFT) erlaubt es mithilfe von Rechenleistung die Eigenschaften einer Vielzahl von Materialien zu bestimmen, sowie Experimente zu bestätigen und spielt somit eine zentrale Rolle in der Festkörperphysik. Um ferroelektrische Phasenübergänge mithilfe von DFT zu untersuchen, wird die sogenannte soft-mode Theorie angewendet. Hierbei deutet das Verschwinden der Frequenz einer soft-mode auf eine Phaseninstabilität hin.

In dieser Arbeit werden strukturelle und elektronische Eigenschaften, sowie Schwingungsmoden von $KTaO_3$ mithilfe verschiedener DFT Methoden untersucht. Die Moden werden durch Veränderung des isotropen Drucks sowie der elektronischen Korrelation berechnet. Letzteres ist mittels Standard DFT schwer erfassbar. Während erster Berechnungen der Schwingungsmoden wurden Moden gefunden, welche auf einen Phasenübergang hindeuten. Aufgrund von diesen Moden wurden durch Variieren des äußeren Drucks im nächsten Schritt Untersuchungen von Phaseninstabilitäten gemacht. Durch Stabilisierung der imaginären Schwingungsmode wurde schlussendlich Kristallstrukturen mit einer niedrigeren Symmetrie als die der Kubischen gefunden. Da die Energiedifferenzen zwischen den ferroelektrischen Strukturen, die aus dieser Methode hervorgehen, und dem paraelektrischen Kristall, gering sind, stützt dieses Ergebnis das quantenparalektrische Modell von $KTaO_3$.

Contents

Chapter 1

Introduction

In this section I cover the theoretical background of this work. The first part deals with the basics of ferroelectricity, and which role phonons play during a ferroelectric phase transition in ionic crystals. In addition, theoretical aspects of displacive phase transitions are presented. Then, perovskite oxides are introduced with a focus on the polar properties of $KTaO_3$. Finally I report the basics of density functional theory, as well as its critical aspects.

1.1 Ferroelectricity

Most materials get electrically polarized by applying an external electric field E. This means that permanent electric dipole moments

$$\boldsymbol{p} = \sum_{i}^{n} q_i \boldsymbol{d}_i \tag{1.1}$$

are induced within the material. Here q_i is the charge of each particle and $\boldsymbol{d}_i$ the distance vector. The dependence of the polarization on the strength of E may differ between different materials. Commonly three different states are distinguished (see Fig. 1.1): First *dielectric polarization* (DE) with a linear dependence on E, then *paraelectric polarization* (PE) which shows a non-linear dependence on E and thirdly *ferroelectric polarization* (FE) that has a nonzero polarization even at E=0. In addition, a ferroelectric material can reverse its polarization and thus shows a hysteresis loop.

The term "Ferro", from Latin *Ferrum*, (*iron*) should indicate the similar behaviours of the spontaneous dipole-moment polarization in ferroelectrics and the spontaneous magnetization in ferromagnets. However, these two concepts originate from quiet different microscopic processes: Ferroelectrics have an asymmetry in *charge* while ferromagnets have an asymmetry in *spin*.

Now consider a displacement of ions from a centrosymmetric PE high symmetry phase, as for example in the perovskite structure, shown in Fig. 1.2 (FE). Here the cation (black) and the oxygen atoms (grey) are displaced in the opposite direction, creating a dipole momentum. Dipole-dipole interaction may lead to a ferroelectric state of the crystal, but in some instances the interactions' tendency to produce long-range ordering is overcome by competing effects. In that case, the dipole moments cancel out, leaving the material unpolarized. This is called *antiferroelectricity* (AFE) and an example is pictured on the right side of Fig. 1.2. Here the oxygen octahedron rotates around the B cation, but the neighbouring unit cells rotate in the opposite direction, thereby the overall structure is non FE.

A convenient approach to characterize a para- to ferroelectric phase transition solely based on the change of symmetry is the *Landau-theory*[1]. It allows us to compare experimental measurable quantities using a minimal set of input parameters which can be obtained

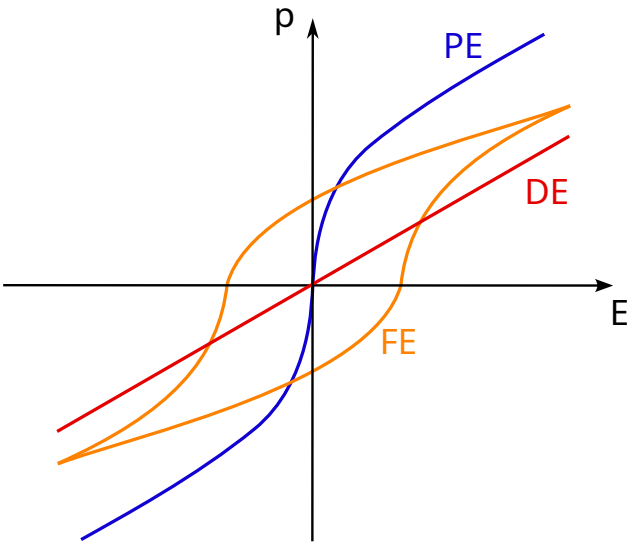

Figure 1.1: *Polarization of dielectric (DE), a paraelectric (PE) and a ferroelectric (FE):* The DE shows a linear dependence of the polarization p on the applied electric field E. For the PE the relationship is non-linear. The FE is distinguished by having a nonzero polarization at zero E.

from first-principle approaches. Thereby the phase transition is characterized by an *order parameter* which is zero at the high symmetry phase and changes to a finite value as the symmetry is lowered. For FE phase transition, the order parameter is the *polarization* P, defined as the dipole momentum per unit cell. Following the work of Landau, the Ansatz is to write the free energy $\mathcal{F}$ as a power expansion of the polarization with the origin chosen to be zero:

$$\mathcal{F}_P = -EP + \frac{1}{2}aP^2 + \frac{1}{4}bP^4 + \frac{1}{6}cP^6,$$

where the power series was truncated at the sixth term. E is the external electric field and a, b, c are coefficients yet to be determined. From the thermal equilibrium at the minima of $\mathcal{F}$, we obtain the *linear dielectric susceptibility* $\chi = P/E = 1/a$. Usually it is assumed that the coefficient a shows a linear temperature dependence, such that $a = a_0(T - T_C)$ where T_C is the *Curie point* (the coefficients b and c are taken to be independent of temperature). What follows is the *Curie Weiss law* for ferroelectrics with temperatures $T > T_C$:

$$\chi = \frac{1}{a_0(T - T_C)}. \tag{1.2}$$

Including the expression for a in the free energy formula, two different cases are distinguished: $a > 0$ ($T > T_C$), the PE phase and $a < 0$ ($T < T_C$), the FE phase. These two cases are schematically shown in Fig. 1.3. At high temperature, the potential has the form of a single well and the structure is PE, but as temperature decreases, the potential changes to a double-well form, the FE structure. In this process, the dielectric constant ε diverges as temperatures are very low. As depicted at the bottom of Fig. 1.3, some materials exhibit another state, called *quantum paraelectric* (QPE). Hereby the material is close to FE, but the transition is suppressed by quantum fluctuations. The free-energy curve of a QPE is expected to have the form of a shallow double well. In this case the structure does not prevent tunneling from one stable polar state to the other. In that case ε is strongly increasing for low temperatures, but finally reaching a plateau. Since the QPE and FE state are very close to each other, it makes materials which experience QPE very sensible to reach FE via external perturbation such as pressure or atomic substitution. [2] This, and the low temperatures challenges the study of QPE systems.

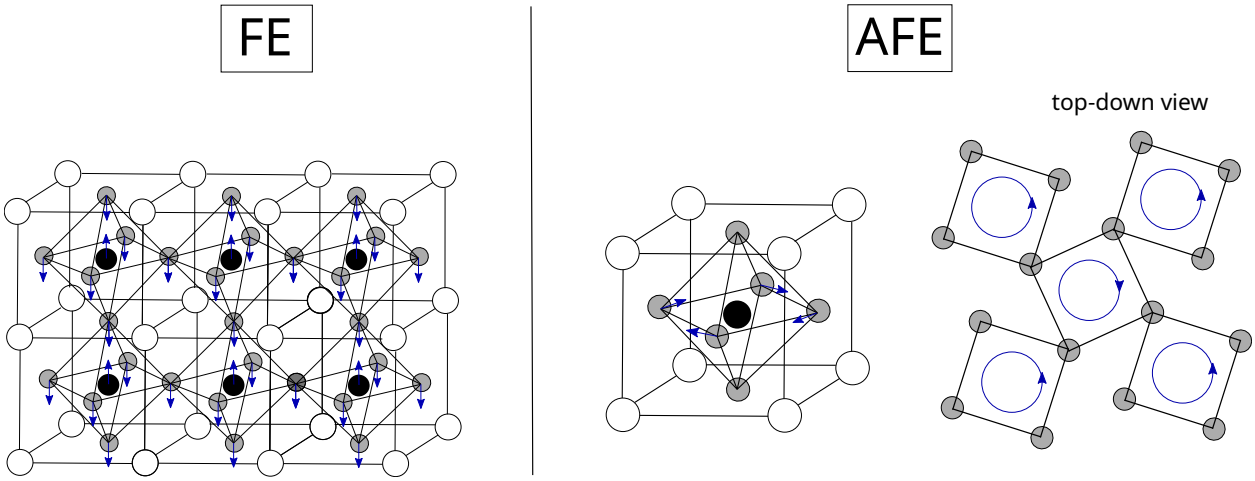

Figure 1.2: *Examples of ferroelectric and antiferroelectric distortions in a perovskite structure:* In the case of FE, the B cation (black) is shifted off center relative to the oxygen atoms (grey). Neighbouring unit cells transform accordingly, leading to a spontaneous polarization of the crystal. For AFE, the oxygen octahedron rotates around the central atom, but the octahedra in adjacent unit cells rotate in the opposite direction, which leaves the final structure nonpolar.

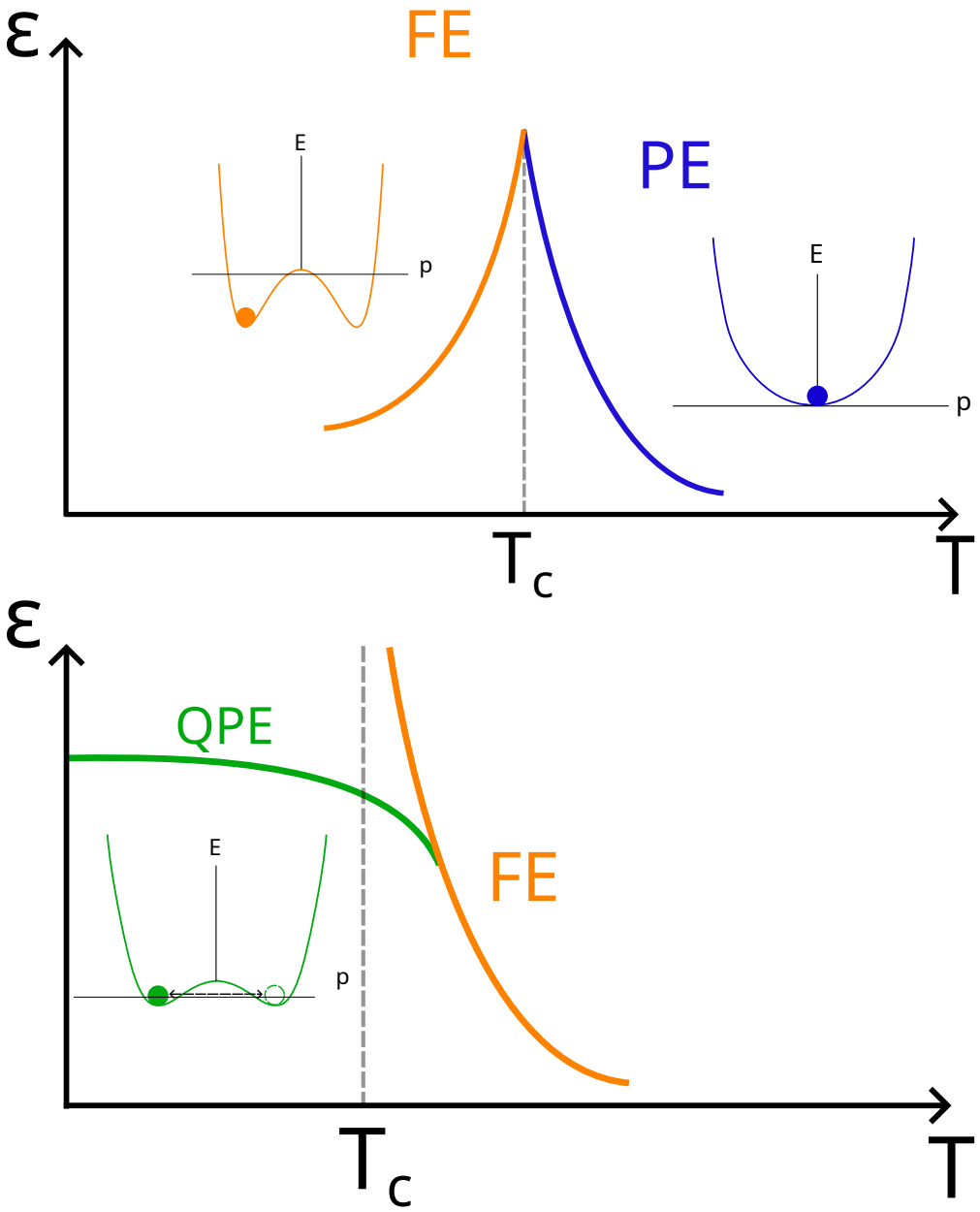

Figure 1.3: *Dielectric constant: paraelectric, quantum paraelectric and ferroelectric.* At low temperatures, when the system is about to reach a FE state, quantum fluctuations may prevent the transition. In that case, the double well is not deep enough to prevent tunneling from the one stable polarization state to the other. Materials in such a state are called quantum paraelectric (QPE). The dielectric constant is expected to reach a plateau for low temperatures.

1.2 Lattice dynamics and soft modes

In this section, the theory of FE phase transition is linked to the lattice vibrations in a crystal via the theory of soft phonon modes.

1.2.1 Phonons in a 3D-crystal

In this section, lattice vibrations of three dimensional crystal structures in the harmonic approximation are discussed [3]. Let us consider any three-dimensional lattice structure with N unit cells, a basis of atoms $\mathbf{d_1}, \mathbf{d_2}, ..., \mathbf{d}_{\nu_b}$ and a translation vector $\mathbf{t}_n$. It is convenient to distinguish between unit cells, which are labelled as a Latin index n and atoms inside a unit cell, denoted as Greek index ν. Therefore $(n\nu)$ means the atom ν in the unit cell n. $\mathbf{u}_{n\nu}$ defines the displacement of a specific nuclei.

Applying the *Born-Oppenheimer approximation*, the nuclei are supposed to be fixed at the positions $\mathbf{t}_n + \mathbf{d}_\nu + \mathbf{u}_{n\nu}$. Since the quadratic terms dominates for small perturbations, it is natural to expand the ground state energy of the electron-nuclei system up to second order. This is well known as the *harmonic approximation* written as

$$E_0(\mathbf{u}_{n\nu}) = E_0(0) + \frac{1}{2} \sum_{n\nu\alpha, n'\nu'\alpha'} \underbrace{\left(\frac{\partial^2 E_0}{\partial u_{n\nu\alpha} \partial u_{n'\nu'\alpha'}} \right)_0}_{D} u_{n\nu\alpha} u_{n'\nu'\alpha'}. \tag{1.3}$$

α,α' each specify a direction x, y or z. Furthermore ν and ν' equal to $1, 2, ..., \nu_b$; $n = 1, 2, ..., N$. It is important to note, that there is no linear term in the expansion since it vanishes at the equilibrium configuration. $D \equiv D_{n\nu\alpha, n'\nu'\alpha'}$ are called the *inner atomic force constants*, evaluated at the equilibrium configuration. The matrix D formed by these force constants is called the *force constant matrix*. The resulting equation of motion of a nucleus ν, experienced due to the potential created by the other nuclei reads as

$$M_\nu \ddot{u}_{n\nu\alpha} = - \sum_{n'\nu'\alpha'} D_{n\nu\alpha, n'\nu'\alpha'} u_{n'\nu'\alpha'}.$$

The translational symmetry in a crystal suggest to consider travelling waves as solutions, so we make the Ansatz

$$\mathbf{u}_{n\nu}(t) = \mathbf{A}_\nu(\mathbf{q}, \omega) e^{i(\mathbf{q}\cdot\mathbf{t}_n - \omega t)},$$

where we call $\mathbf{A}_\nu(\mathbf{q}, \omega)$ the *polarization vectors* of vibrations of the nuclei. It follows that

$$-M_\nu \omega^2 A_{\nu\alpha} = - \sum_{n'\nu'\alpha'} D_{n\nu\alpha, n'\nu'\alpha'} e^{-i\mathbf{q}\cdot(\mathbf{t}_n - \mathbf{t}_{n'})} A_{\nu'\alpha'}.$$

To get the non-trivial solutions, the determinant of the coefficients in the above equation has to vanish, i.e.

$$det \left(\sum_{n'} D_{n\nu\alpha, n'\nu'\alpha'} e^{-i\mathbf{q}\cdot(\mathbf{t}_n - \mathbf{t}_{n'})} - M_\mu \omega^2 \delta_{\alpha\alpha'} \delta_{\nu\nu'} \right) = 0. \tag{1.4}$$

For each $\mathbf{q}$, this equation produces $3\nu_b$ eigenvalues, called *phonons* or *normal modes* (for abbreviation they are also called modes). This insight decouples any complex coupled oscillatory motion in one particular coordinate system, into a set of simple harmonic motions in another coordinate system.

In general two type of modes are distinguished: *longitudinal* and *transversal*. For the former mode, the direction of $\mathbf{A}_\nu(\mathbf{q})$ is parallel, for the latter it is perpendicular to $\mathbf{q}$. Now

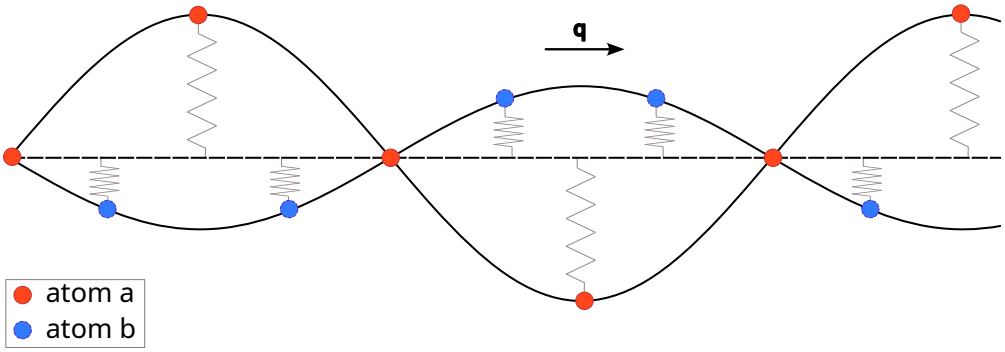

Figure 1.4: *Transversal optic (TO) mode of a diatomic chain:* The two different atomic species (red and blue) move perpendicular to the wave vector q, and out-of-phase. The springs to which the atoms are connected represent the displacements from their position of rest.

consider the long wavelength limit ($\mathbf{q} \to 0$) of the determinantal equation (1.4). From the fact that the forces do not only vanish if the nuclei displacements are zero, but also when all displacements are equal, it follows that the sum of any row or the sum of any column of the dynamical matrix vanish. Also taking equation (1.4) into account, it follows

$$\sum_{\nu'} D_{n\nu\alpha,\nu'\alpha'}(\mathbf{q}=0) \equiv 0,$$

and in particular

$$\sum_{\nu'\alpha'} D_{n\nu\alpha,\nu'\alpha'}(\mathbf{q}=0) A_{\alpha'} \equiv 0.$$

This shows that vibrations with amplitudes $A_{\nu'\alpha'} = A_{\alpha'}$ are the same for all atoms of a basis satisfying equation (1.4) with $\omega = 0$. Thus every three-dimensional crystal has three *acoustic* modes, with the frequency approaching zero, as the wave vector goes to zero. For these cases, the atoms are vibrating in phase and with the same amplitude in a particular unit cell. The remaining $3\nu_b - 3$ vibrations, called *optical modes*, leave the motion of the center of mass in a cell unaltered. Fig. 1.4 illustrates a transversal optic phonon modes in a diatomic chain. Here the forces are represented as simple springs and the two different atomic species move out-of-phase and perpendicular to the wave vector.

In the following section the theory of soft modes is explained which builds the bridge between phonons and phase transitions in crystals.

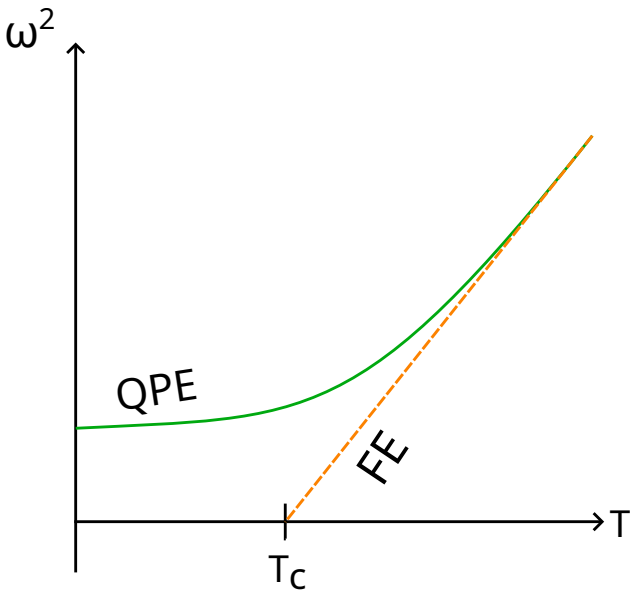

Figure 1.5: *TO soft mode for a paraelectric and a ferroelectric:* When temperatures reach the Curie point, the phonon soft mode associated with the phase transition goes to zero in case of a ferroelectric (straight dashed orange line), and approaches a low frequency value for the quantum paraelectric phase (green line).

1.2.2 Polar vibrations

Take a crystal slab where all the positive ions are displaced by the same amount perpendicular to the slabs faces. In addition all negative ions are shifted in the opposite direction. This introduces an effective charge e^* of an ion. In this case, e^* defines the ratio of the dipole momentum per ion pair induced in the slab by such a displacement, to the relative displacements of the negative and positive ions. For this system, Lyddane, Sachs and Teller [4] found a simple expression for the longitudinal ω_{LO} and transversal ω_{TO} vibration frequency in terms of the static dielectric constant ε of the crystal

$$\frac{\omega_{LO}^2}{\omega_{TO}^2} = \frac{\varepsilon}{\varepsilon_0},$$

where ε_0 is the dielectric constant for frequencies in the visible range.

In particular the formula is independent of e^* and true for any other geometric shape of the crystal. As ε is proportional to χ, it follows that $\omega_{TO} \to 0$ signals a phase transition [5]. It follows that

> The anomalously large dielectric constant associated with a phase transition is directly related to a low-frequency transverse optic soft mode.

The relationship is schematically shown in Fig. 1.5. For a FE, the frequency ω^2 goes to zero at the Curie temperature T_C. In contrast to a quantum paraelectric for which the mode softens, but its frequency reaches a non-zero value (see bottom of Fig. 1.3 for the corresponding behavior of ε). .

As phase transitions in crystals are always accompanied with a change in symmetry, group theory comes in handy to predict possible symmetry relations between the crystal structure of the high- and the low-symmetry phase, without considering any physical interactions. In the forthcoming section I will explore this topic.

1.3 Symmetry analysis of normal modes

A structural phase transition is accompanied with a loss of symmetry. If the *parent phase* of a crystal has space group G, after the transition the crystal has space group G' which is a subgroup of G. Landau describes such a structural phase transition due to the condensation of a set of collective degrees of freedom, which transform according to an *irreducible representation* (IR) of the space group of the parent phase. The following introduction closely follows the work of Stokes, Hatch and Wells. [6]

Consider a vector space S of displacements of N atoms. This space is $3N$ dimensional. Now we take one particular displacement vector $\boldsymbol{\phi} \in S$ and act on it with all elements of a space group G. This obviously induces a subspace S' of S for which we define a set of n basis vectors $\boldsymbol{\phi}_j$. The action of any $g \in G$ on any of these vectors can be written as a linear combination of other basis vectors with $n \times n$ matrices D_{jk} as coefficients:

$$g\boldsymbol{\phi}_j = \sum_{k=1}^{n} \boldsymbol{\phi}_k D_{kj}(g) \tag{1.5}$$

A minor calculation shows that the mapping from g onto $D(g)$ is a *representation* of the group G. Taking a displacement vector orthogonal to every vector in S', we can repeat the procedure and find another subspace S'' of S which does not overlap with S'. We can continue until the whole space S is decomposed into orthogonal subspaces.

If there is some vector $\boldsymbol{\phi}'$ in the n-dim space S' such that the set of vectors $\{g\boldsymbol{\phi}'\}$ span a subspace with dimension $< n$, then S' is reducible and can further be decomposed into subspaces. This process can be continued until each subspace is associated with a set of matrices $D(g)$ which are IRs of G.

Assume again that a displacement of atoms typically lowers the symmetry of the crystal from G to G'. Considering every subgroup G' one at a time, there may be several vectors $\boldsymbol{\phi}$ of S' which lead to the same subgroup, representing themselves a subspace of S'. Collecting these vectors we get a subspace S'' of S' which is invariant under operations g of some subgroup of G. These subgroups are called *isotropy subgroups*, each belonging to the IR of S'. Writing every vector of S' as a linear combination of basis vectors, with coefficients η_i, we can consider the operation of g on $\boldsymbol{\eta}$ instead of the basis vector $\boldsymbol{\phi}_j$. $\boldsymbol{\eta}$ can be considered as a vector in representation space and called *order parameter*.

Summarizing, given an IR, we can now determine all possible isotropy subgroups by forming vectors $\boldsymbol{\eta}$ in representation space. The whole procedure is done without specifying any atomic positions.

In practice, the IR corresponding to a phase transition is identified using basic group theoretical methods. Then the decomposition into irreducible subspaces is usually done in the following way:

1. Generate a list of IRs

2. For each IR, try to find an (invariant) subspace of representation space where $\boldsymbol{\eta}$ satisfying
$$D(g)\boldsymbol{\eta} = \boldsymbol{\eta}. \tag{$*$}$$

3. If such $\boldsymbol{\eta}$ are found, then we check for additional g in G which are not in G' also satisfying equation $(*)$.

4. All the operators that satisfying equation $(*)$ constitute a isotropy subgroup G'' which is associated with the IR.

Subgroup	Dir
P4mm (99)	(a,0,0)
Amm2 (38)	(a,a,0)
R3m (160)	(a,a,a)
Pm (6)	(a,b,0)
Cm(8)	(a,a,b)
P1(1)	(a,b,c)

Table 1.1: Isotropy subgroups for the IR Γ_4^- of Pm$\bar{3}$m and the direction of the order parameter (Dir).

5. Well known group theoretical methods are applied to generate the subspaces of S associated with the IR and thus the atomic displacements for $\boldsymbol{\eta}$.

For example, the space group Pm$\bar{3}$m has 10 IRs associated with the Γ point of the Brillouin zone. Taking the IR Γ_4^-, there are six non-equivalent invariant subspaces of the representation space of Γ_4^- defined by the vectors $\boldsymbol{\eta}$ =(a, 0, 0), (a, a, 0), (a, a, a), (a, b, 0), (a, a, b), (a, b, c) with arbitrary constants a $\neq$ b $\neq$ c . If we take $\boldsymbol{\eta}$ =(a, 0, 0) as an example, there are eight matrices satisfying $g\boldsymbol{\eta} = D(g)\boldsymbol{\eta}$:

$$D_{1,2,3,4}(g) = \begin{pmatrix} 1 & 0 & 0 \\ 0 & 0 & \pm 1 \\ 0 & \pm 1 & 0 \end{pmatrix}, \quad D_{5,6,7,8}(g) = \begin{pmatrix} 1 & 0 & 0 \\ 0 & \pm 1 & 0 \\ 0 & 0 & \pm 1 \end{pmatrix}.$$

We can check the character table to find the operators g which maps Γ_4^- onto these matrices. With the operators we can identify the isotropy subgroup, which is $P4mm$ in this case. For for the other vectors $\boldsymbol{\eta}$ this is done in an analogous way and the resulting subgroups are listed in Table 1.1.

In the following section I give an overview of the material studied in this work.

1.4 Perovskite ABO_3 materials

Perovskites are materials with a crystal structure ABX_3 where 'A' and 'B' are cations and 'X' is an anion. They exhibit an exceptional range of interesting physical properties like ferroelectricity, superconductivity, charge ordering or spin-dependent transport. The ability of a FE perovskite to switch between the two stable polarization state provides a basis for applications like nonvolatile random-access memories: Boolean algebra's "0" or "1" are stored as either a "+" or a "-" state in the memory cell. As FE manifest pyroelectricity and piezoelectricity, an even more wide range of different possible applications open.

$BaTiO_3$ is a prototypical ferroelectric, undergoing a phase transition, first to a tetragonal structure and then, by subsequently lowering the temperature, to an orthorhombic and a rhombohedral phase. $SrTiO_3$ on the other hand, show strong signs of undergoing an antiferrodistortive structural phase transition by an rotation of TiO_6 octahedron around the unit cell axes. [7] (see Fig. 1.2)

$KTaO_3$ (KTO), another perovskite structure, remains in a paraelectric cubic phase down to lowest temperatures. However, early measurements have shown a peak of the dielectric constant at around 10 K[8], a sign of an ongoing phase transition (see Fig. 1.6). It is expected that the resulting ferroelectric structure is tetragonal. Although subsequent experiments lack any evidence for a transition [9] other experimental measurements (e.g. [10]) indicated anomalies of some phonon modes around 10 K. Since then, a great variety of experiments

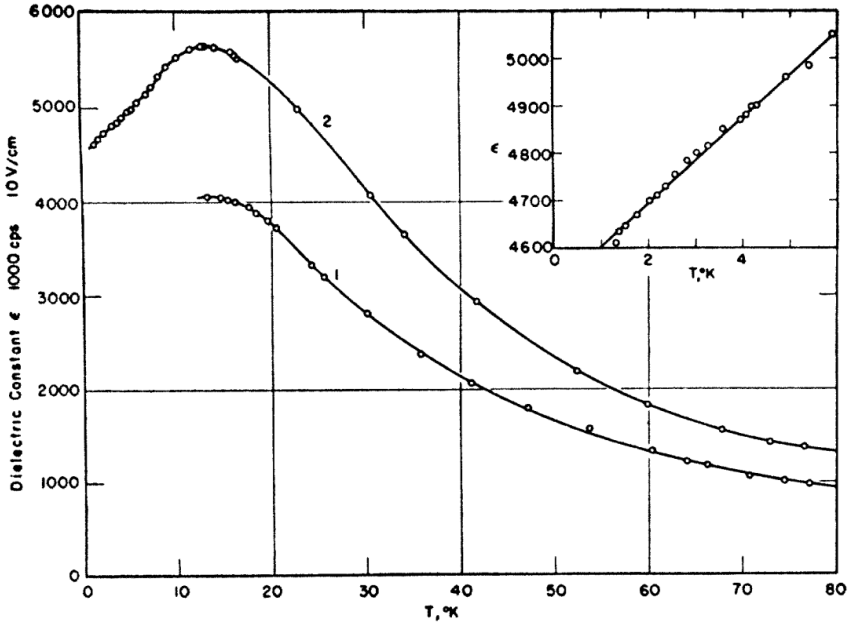

i

Figure 1.6: *Dielectric constant of KTO:* Early measurements show a peak at around 10 K. Image adapted from Ref. [8].

and simulations were executed to unveil the FE behavior of KTO. Nowadays KTO is mostly referred as quantum paraelectric, but it is still not entirely clear if a FE transition occurs under external perturbations such as pressure or strain.

This work aims to contribute for a better understanding of FE within KTO by computing the phonon modes, with a focus on the transversal optic FE soft mode (TO1). Thereby I use mainly two different approaches withing the framework of density functional theory: First applying isotropic pressure, e.g. changing the lattice volume of the cubic structure, and secondly introducing a correction to the electronic correlation in form of an U parameter. The structural investigation is accompanied by electronic calculations, revealing the band gap and band structure of KTO.

In the next section, I focus on the theory concerning the computational part of this thesis.

1.5 Density functional theory

A solid consists of a large number of electrons and nuclei mutually interacting with each other. A simplified, yet often adequate description assumes an instantaneous and spin-independent Coulomb interaction between particles, characterized by the following total Hamiltonian

$$H_{tot} = \underbrace{\sum_i \frac{\mathbf{p}_i^2}{2m} + \sum_I \frac{\mathbf{p}_I^2}{2M}}_{(1)} + \underbrace{\sum_i V_{nuc}(\mathbf{r}_i)}_{(2)} + \underbrace{\frac{1}{2}\sum_{i\neq j} \frac{e^2}{|\mathbf{r}_i - \mathbf{r}_j|} + \frac{1}{2}\sum_{I\neq J} \frac{z_I z_J e^2}{|\mathbf{R}_I - \mathbf{R}_J|}}_{(3)},$$

where

$$V_{nuc}(\mathbf{r}) = -\sum_I \frac{e^2 z_I}{|\mathbf{R}_I - \mathbf{r}|}.$$

Each term has the following physical interpretation:

(1) Kinetic energy of electrons with mass m and nuclei of mass M.

(2) Attractive potential energy between electrons and nuclei.

(3) Electron-electron and nucleus-nucleus repulsive potential energy

The exclusion of self interaction is indicated as $i \neq j$ for the electrons and as $I \neq J$ for the nuclei. The large difference between the electron and the nuclear masses suggests to neglect the kinetic energy of the nuclei. As a result, the second term in the total Hamiltonian can be dropped, and the nuclei positions $\mathbf{R}_I$ can be considered in a fixed configuration and are dropped as well. It follows that H_{tot} can be rewritten as a Hamiltonian H_e of N interacting electrons in the presence of nuclei in some fixed configuration.

The goal is now, to find a solution to the *Schrödinger equation*

$$H_e \ \Psi(\mathbf{r}_1, \mathbf{r}_2, ..., \mathbf{r}_N) = E \ \Psi(\mathbf{r}_1, \mathbf{r}_2, ..., \mathbf{r}_N) \tag{1.6}$$

where Ψ is the N-electron wave function. While solutions using one-electron approach were proposed by Hartree and Fock, a pioneering approach was made with the conceptual shift from the ground state wave function to the ground state one-body *electron density* $\mathbf{n}(\mathbf{r})$. This defines the basis of *density functional theory* (DFT).

1.5.1 Hohenberg-Kohn and Kohn-Sham

The two Hohnberg-Kohn theorems [11] are the backbone of DFT. The first one states the following:

> There is a one to one correspondence between the ground state electronic density $\mathbf{n}(\mathbf{r})$ and the external potential $V_{nuc}(\mathbf{r})$.

Thus from the knowledge of the electronic ground-state density $n(\mathbf{r})$ the external potential is in principle uniquely determined (except an arbitrary constant). Furthermore, by solving the Schrödinger equation, the ground state wave function can be determined.

After Hohenberg and Kohn, the ground state energy is constructed the following way:

$$E_{HK}[n(\mathbf{r}), V_{nuc}(\mathbf{r})] \equiv T[n(\mathbf{r})] + V_{ee}[n(\mathbf{r})] + \int V_{nuc}(\mathbf{r}) n(\mathbf{r}) d\mathbf{r} \tag{1.7}$$

where $V_{nuc}(\mathbf{r})$ is taken constant and $n(\mathbf{r})$ can vary. By a variational principle, it can be shown that

> The unique functional (1.7) is minimal at the exact ground-state density.

This fact is known as the *second Hohenberg-Kohn theorem.*

Unfortunately $T[n] + V_{ee}[n]$ is not known, so the problem of finding an appropriate approximate functional remains. Kohn and Sham [12] invented a strategy which defines the standard underlying scheme for DFT calculations nowadays. It relies on the following important property:

> For every non-uniform ground state density $n(\mathbf{r})$ of an interacting electron system, there exists a non-interacting electron system with the same ground state density $n(\mathbf{r})$.

This brings the consequence, that the ground-state density $n(\mathbf{r})$ of an interacting N-electron system can be decomposed into a sum of N independent orthonormal orbital contributions

$$n(\mathbf{r}) = \sum_i \phi_i^*(\mathbf{r})\phi_i(\mathbf{r}).$$

Recasting E_{HK} by extracting the electron Coulomb interaction (Hartree potential V_H) and the kinetic energy T_0 of the system of non-interacting electrons with the same density gives

$$E_{HK}[n(\mathbf{r}), v_{ext}(\mathbf{r})] \equiv T_0[n(\mathbf{r})] + V_H[n(\mathbf{r})] + \int v_{ext}(\mathbf{r})n(\mathbf{r})d\mathbf{r} + E_{XC}[n(\mathbf{r})]$$

where

$$E_{XC}[n(\mathbf{r})] = T[n(\mathbf{r})] - T_0[n(\mathbf{r})] + V_{ee}[n(\mathbf{r})] - V_H[n(\mathbf{r})] \tag{1.8}$$

is called the *exchange-correlation functional* (XC). By variation of E_{XC} with respect to a set of orbitals, we obtain the famous *Kohn-Sham equations*

$$\left[-\frac{\hbar^2\nabla^2}{2m} + V_{nuc}(\mathbf{r}) + V_H(\mathbf{r}) + V_{XC}(\mathbf{r})\right]\phi_i(\mathbf{r}) = \epsilon_i\phi_i(\mathbf{r}). \tag{1.9}$$

The problem that E_{XC} is not known, remains. Nevertheless, since the advent of DFT, a great amount of different exchange-correlation functionals were proposed. In the following section, the functionals most frequently used in today's DFT calculations are described.

1.5.2 LDA, GGA and Meta GGA

In the early work of Hohenberg and Kohn, a simple exchange-correlation functional for slow varying electron density was given. [12] as

$$E_{XC}^{LDA}[n(\mathbf{r})] = \int n(\mathbf{r})\epsilon_{XC}(n(\mathbf{r}))d\mathbf{r},$$

where $\epsilon_{XC}(n(\mathbf{r}))$ is the exchange-correlation energy per electron of a uniform interacting electron gas with density $n(\mathbf{r})$. This functional is called the *local density approximation* (LDA).

While LDA thought to be best suited for systems where the electron density slowly varies, such as free electron metals, it is also surprisingly successful in describing molecules or semiconductors. However it leads to very inaccurate cohesive energies ($20\% - 30\%$) and underestimates lattice constants (up to 5%).[13]

A natural extension of LDA is to take the change in the electron density into account. Such functionals are called *generalized gradient approximations (GGA)* or semi-local density functional approximations and take the following form:

$$E_{XC}^{GGA}[n(\mathbf{r})] = \int n(\mathbf{r})\epsilon_{XC}\left(n(\mathbf{r}), |\nabla n(\mathbf{r})|\right) d\mathbf{r}.$$

The *Perdew-Burke-Ernzerhof (PBE)* GGA is one of the most widely used functional in DFT, evidenced by the fact that its paper is the 16-th most cited scholarly article of all time [14, 15].

A modified version of PBE is *PBEsol*, designed to improve upon PBE in equilibrium properties of solids, in the bulk, as well as on the surface. [16] PBEsol differs only in two parameters from PBE, and in contrast to PBE contains the second-order gradient expansion for exchange. This leads to a better prediction of lattice constants than PBE, however the cohesive energies are less accurate [17, 18].

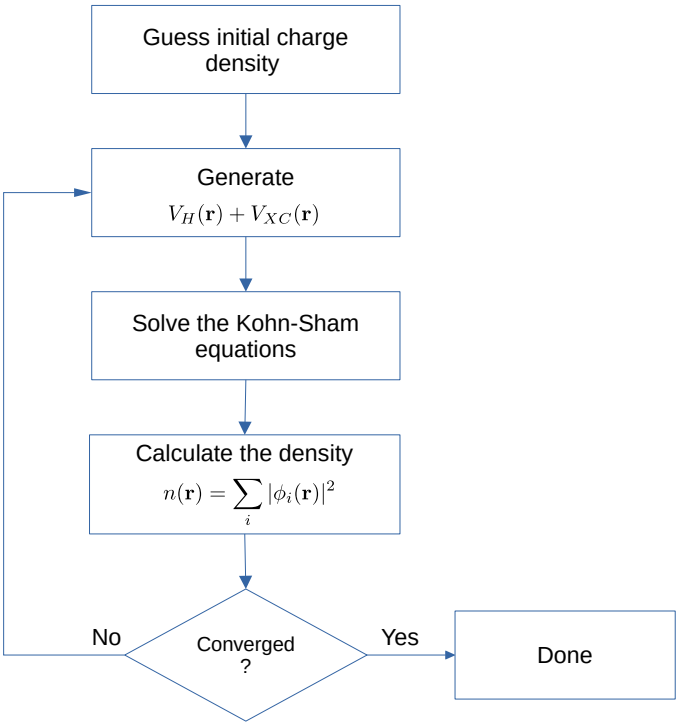

Figure 1.7: The self-consistent procedure of a DFT calculation.

Another approach is made by the so called *META-GGA* functionals [19], which in addition to GGA, include the second derivative of the electron density. Similarly as before, we write

$$E_{XC}^{MGGA}[n(\mathbf{r})] = \int n(\mathbf{r})\epsilon_{XC}\left(n(\mathbf{r}), |\nabla n(\mathbf{r})|, |\triangle n(\mathbf{r})|\right) d\mathbf{r}.$$

The *strongly constrained and appropriately normed* (SCAN) META-GGA proposed in 2015 [20] satisfies all 17 known exact constraints that a META-GGA can fulfill. For many cases SCAN is more accurate than other GGA functionals and can be equally accurate as hybrid functionals, with the advantage of lower computational cost.

1.5.3 DFT+U

As mentioned in section 1.5.2, DFT simulations using LDA, GGA or META-GGA functionals, typically fail to deliver correct predictions of some physical quantities. A common example is the lattice structure for specific materials, including the perovskite oxides under study here. This failure can be traced back to an inaccurate description of the charge localization at atomic sites. Problems like delocalization of excess charges overall in the lattice, or partial occupations of energy levels instead of integer occupations, remain to be resolved.

It is expected that the exact total energy is a linear function of the electronic occupation, which is discontinuous in the first derivative for integer occupations, thus $d^2E/dn_i^2 = 0$ except at integers $N = n_i$. This means that during adding and removing electrons, the energy of state i is stays constant. LDA, GGA and META-GGA in contrast result in a non-linear behavior of E such that $d^2E/dn_i^2 > 0$. As a result, the self-interaction effect leads to a preferred partial occupation, instead of integer occupation. This introduces problems like underestimation of the energy gap, identifying strongly-correlated insulators as metals, or failing to account for charge localization.

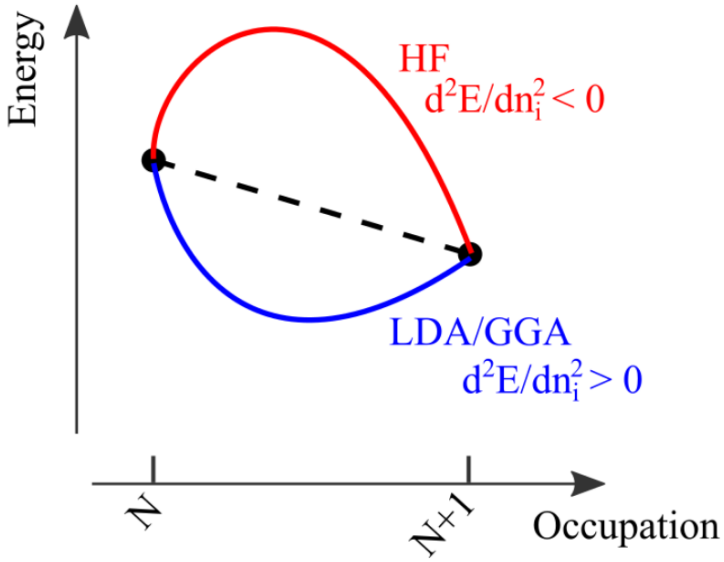

Figure 1.8: *The total energy vs. the electronic occupation number:* DFT implemented as LDA or GGA have a convex form, while Hartree Fock (HF) schemes show concave behaviour. Image adapted from Ref. [21].

Different modifications of the exchange-correlation approximations were introduced, such as the hybrid functionals, which mix LDA or GGA with an Hartree Fock (HF) exchange. HF theory predicts the exact opposite as DFT in terms of occupation numbers: The energy change dependent on the occupation has a concave form, $d^2E/dn_i^2 < 0$, thus overestimating the charge localization. The two opposing behaviours are schematically shown in Fig. 1.8.

Another approach is the so called *DFT+U* method which has the advantage of considerably lower computational cost compared to the hybrid approach. The basis of DFT+U is to treat the on-site Coulomb interaction of localized electrons by adding an additional Hubbard-like term, which is either calculated from first principles, or tuned until reaching empirical agreement. DFT+U works as DFT for describing the valence electrons, and differs from DFT in treating the strongly correlated electronic states (d and f orbitals). The total energy of a system is expressed as

$$E_{DFT+U}[n(\mathbf{r})] = E_{DFT}[n(\mathbf{r})] + E_{Hub}[n^{I\sigma}_{mm'}] - E_{dc}[n^{I\sigma}],$$

where $n^{I\sigma}_{mm'}$ is the electron occupation number. Since E_{Hub} is additive, it introduces a double counting (dc) error for the correlated states that has to be subtracted.

The double-counting term E_{dc} is not uniquely defined and different formulations were developed for various circumstances. A frequently used approach was introduced by Dudarev [22], which is invariant under rotation of the atomic orbital basis set used to define the occupation numbers $n_{mm'}$. It takes the following form:

$$E_{DFT+U}[n(\mathbf{r})] = E_{DFT}[n(\mathbf{r})] + \frac{U-J}{2}\sum_{\sigma}\left(\sum_{m} n^{I\sigma}_{mm} - \sum_{m,m'} n^{I\sigma}_{mm'}n^{I\sigma}_{m'm}\right).$$

Within this approach instead of one interaction parameter U, an effective potential U_{eff} =U−J is introduced, where J accounts for Hund's rule coupling. In literature, U_{eff} is simply referred to as "U" which is also adopted in this work.

Chapter 2

Methods

This chapter introduces the methods used for computing the phonons of KTO. The phonons, which account for the main part, are accompanied with a detailed study of the relaxed lattice parameter and the electronic properties. Finally, a group theoretical approach is made to investigate a ferroelectric phase transition.

The *Vienna Ab initio Simulation Package* (`VASP`) [23–26] was adopted to conduct DFT calculations on the Vienna Scientific Cluster 3. Furthermore, the following tools were used for file preparation and post-processing:

- `phonopy`: generate supercells; mode analysis and plotting phonon dispersions.[27]
- `ISODISTORT`: create lattice distortions.[28]
- `AMPLIMODE`: analyze total distortion.[29, 30]
- `sumo`: plotting electronic band structures and phonon dispersions. [31]
- `Python` and `Mathematica`: post-processing.

2.1 Computational Setup: Energy convergence

Before investigating material properties via DFT, it is of outermost importance to ensure that the computational setup is sufficient enough. There are two important parameters to consider: First, the reciprocal space sampling and secondly the plane wave energy cutoff. The homogeneous sampling grid was chosen to be $\Gamma-$ centered. The convergence tests were carried out using the experimental lattice constant and the functionals SCAN, PBE, PBEsol, LDA as well as the screened hybrid functional by Heyd-Scuseria-Ernzerhof (HSE06 [32], denoted simply as HSE). As seen on top of Fig. 2.1, for a 5 atoms ABO_3 cubic unit cell of $KTaO_3$, a sampling size of 8 points in each direction is sufficient for all different functionals, also including the computationally demanding HSE. Furthermore, an energy cutoff of 600 eV is enough for the GGA functionals and HSE as seen in the right of Fig. 2.1. SCAN on the other hand requires a higher cutoff of about 800 eV. The study of the electronic and structural properties was continued with a converged setup of 8 points in each direction and an energy cutoff of 600 eV for GGA/LDA, and 800 eV for SCAN, respectively.

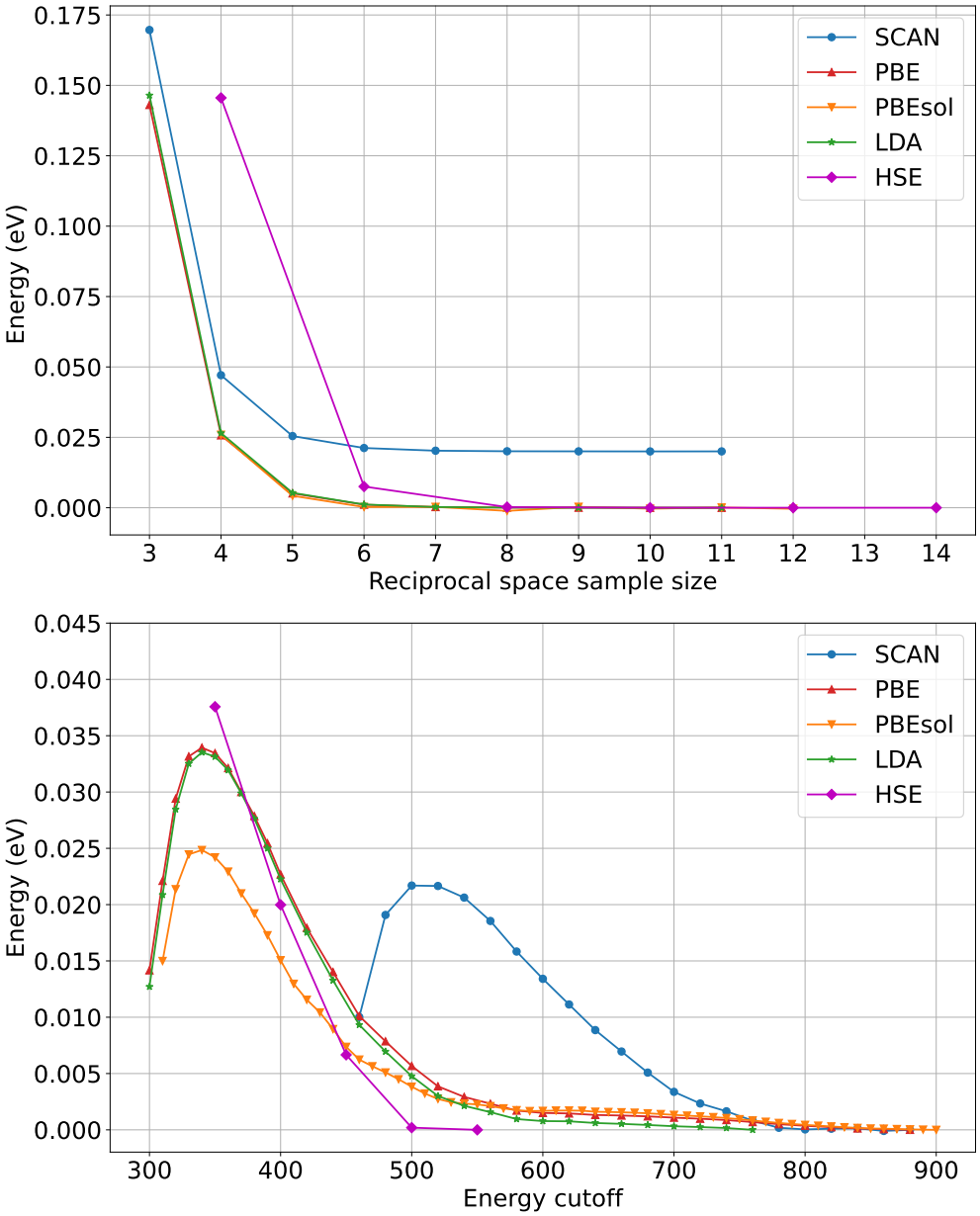

Figure 2.1: *Energy convergence*: Γ− centered reciprocal space sampling (top) and different energy cutoff (bottom). For illustrative purpose, instead of the total energies, the difference between each energy value and the converged energy value is shown.

2.2 Structural and electronic properties

No noticeable difference in structural or electronic properties was found by applying U value to the O, or to the K atoms. This was expected, since O and K do not have d-orbitals which are strongly affected by electronic correlation. Thus in the following, U was applied just for the Ta atom.

The relaxation procedure and the electronic band gap calculations were carried out using the functionals SCAN, PBE, PBEsol and LDA within cubic KTO.

For geometric relaxation, the lattice constant was varied around the experimental value of 3.984 Å (obtained by x-ray diffraction measurements [9]) and the resulting data was fitted with the Birch-Murnaghan equation of state [33].

The electronic band gap was obtained from the energy difference between the highest occupied orbital and the lowest unoccupied orbital of KTO. Spin orbit coupling (SOC) was introduced where indicated, to account for relativistic effects. Electronic band structures were computed via non-self consistent calculations for SCAN, PBE and PBEsol only, with zero U and with U=4 eV.

2.3 Phonons

2.3.1 Computational setup

Phonon dispersions were acquired within the theoretical framework of *finite displacements* of atoms using `VASP` and `phonopy`. Hereby the force constant matrix is evaluated via DFT by displacing each atom in a unit cell by a small distance and calculating the resulting forces on every other atom in the crystal.

Since the overall performance (structural and electronic) of SCAN compared to the other functionals is in better agreement with experimental results, SCAN was mainly used to study phononic properties. In the last section, LDA and PBEsol are also included.

To ensure that the forces between distant atoms go to zero, a sufficiently large cell is needed. Thus I compared phonon dispersions for different sizes of supercells, constructed from the relaxed unit cell. A larger supercell requires less points to sample the reciprocal space, therefore convergence tests using different sampling sizes were executed as well. For this, SCAN + U=5.4 eV was adopted. Fig. 2.2 (top) shows dispersion relations using a $2 \times 2 \times 2$ and a $4 \times 4 \times 4$ supercell, each computed using 2 sampling points in each direction. The most noticeable difference within the modes is around the Γ point. The bottom image of Fig. 2.2 shows the change in sampling size for a fixed $2 \times 2 \times 2$ supercell. Clearly only one point in each direction is not sufficient enough, but between a $2 \times 2 \times 2$ and $4 \times 4 \times 4$ sampling size there is only a small discrepancy, mostly confined to modes at the Γ point. To save computational resources and time, for the qualitative comparison of phonon dispersions, a minimal setup consisting of a $2 \times 2 \times 2$ supercell and a $2 \times 2 \times 2$ reciprocal space sampling was adopted.

2.3.2 SCAN: Change of U and lattice constant

At first, phonon calculations with the experimental and relaxed geometries were performed and compared, excluding any U. It is expected that the phonon dispersion relation is highly sensitive to a change of the lattice parameter as well as the U, especially at the Γ point. Therefore, in the next step the system was confined to a change of lattice constant, as well as U. Dispersions using SCAN and the experimental unit cell with a U-value of 1, 3 and 5.4 eV were compared with the previously determined plots without U. Next, I increased the size

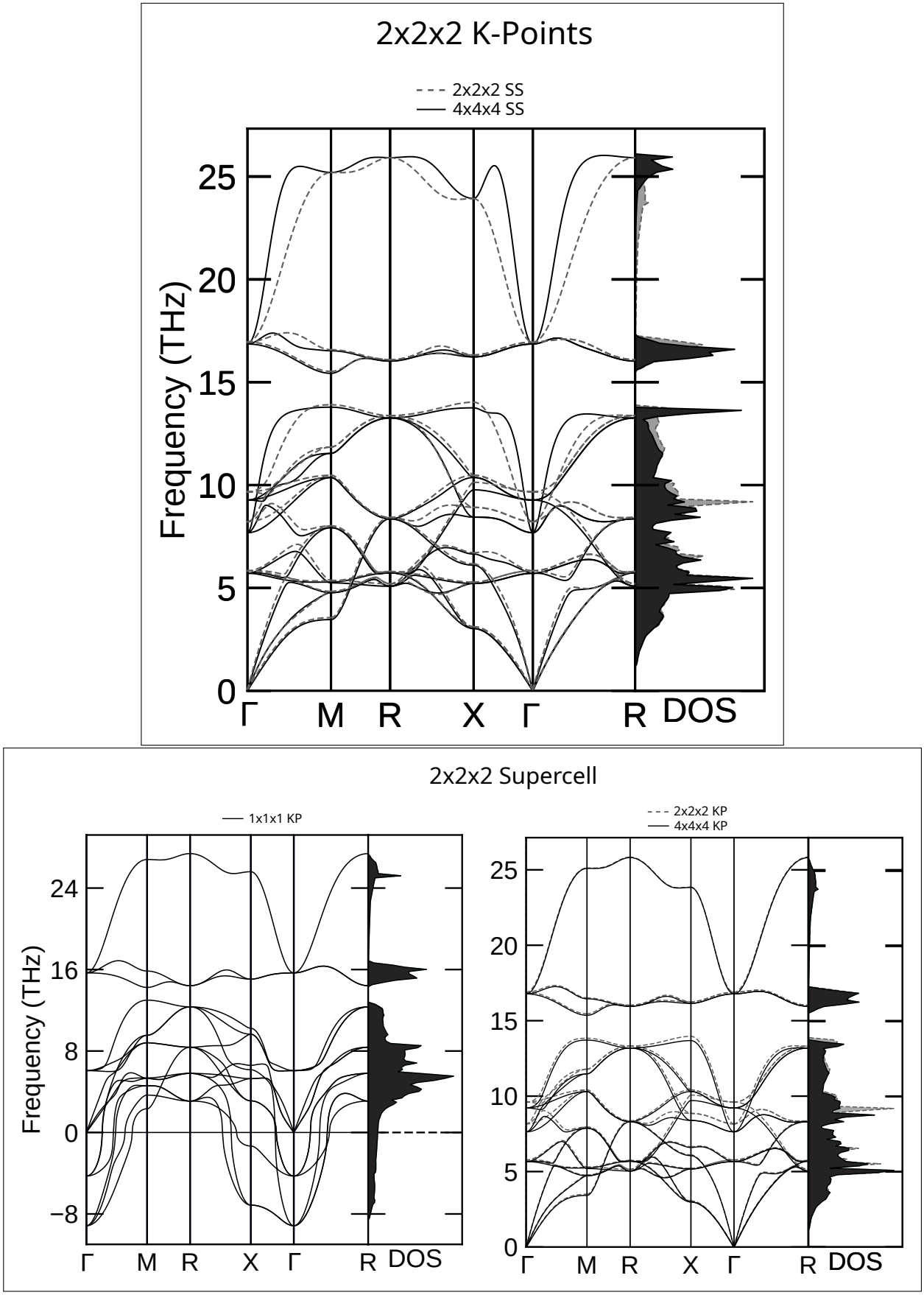

Figure 2.2: *Phonons: Size of supercell and number of k-points.* SCAN+U=5.4 phonon dispersions; Top: With a k-points mesh of $2 \times 2 \times 2$, the phonons were calculated in a $2 \times 2 \times 2$ and a $4 \times 4 \times 4$ supercell. Bottom: Using a $2 \times 2 \times 2$ cell and k-meshes of $1 \times 1 \times 1$, $2 \times 2 \times 2$ and $4 \times 4 \times 4$.

of the lattice constant in steps of around 0.01 Å, starting from the experimental value. For each setup, using a fixed U value of 2 eV, the dispersions were computed and then compared.

The study of phonons was carried on in more detail with a focus on the mode which shows the highest change in frequency during volume- and U-variation. Via phonopy I identified this mode as one of the three triply degenerate transversal optic phonon modes with IR Γ_4^-, referred to as TO1. It corresponds to an opposite movement of the oxygen octahedron and the tantalum atom. The lattice parameter was varied between 3.96 and 4.02 Å, mostly in steps of 0.01 Å. For each such cell size, the U_{Ta} value was chosen between 0 and 3.0 eV, mostly increased in steps of 0.5 eV. For every configuration, the phonon dispersion was plotted and the frequency of the TO1 mode was identified as imaginary or real. Furthermore for each setup, the electronic band gap was determined, as described in section 2.2.

Next, I studied the softening of the TO1 mode in more detail by varying the lattice parameter and the U value closer to the transition point, at which the mode frequency approaches zero. Furthermore, besides SCAN, the functionals PBEsol and LDA are used.

2.3.3 SCAN vs. PBEsol vs. LDA

The phonon dispersions using PBEsol and LDA were compared with the data obtained by using SCAN. Each computation was set up with the relaxed lattice constants and without including U. An additional convergence test for the two functionals was omitted, and I used the same computational setup as with SCAN. Dispersion relations were checked for suspicious phonon modes, which could potentially arise from an insufficiently converged setup.

In addition, a variation of the lattice constant a_0 with PBEsol and LDA was carried out, fixing U. The range of a_0 was confined to values at which the TO1 mode softens to zero for all three functionals.

2.4 Stabilizing the imaginary mode with SCAN

The main unstable phonon mode transforming as the IR Γ_4^- was investigated to search for a energetically favorable ground state structure. Group theory methods were applied within `ISODISTORT` to displace the cubic structure according to the imaginary mode for different directions of the order parameter. For this procedure, a python code by Jiangang He [1] was adopted. In practice, this analysis was carried out via the following steps:

1. Preparing the input file by specifying the structural information as well as the IR and the direction of the order parameter. Then generating the displaced structural files.
2. Executing a static DFT phonon calculation.
3. Reading the forces from the output file, building the force constant matrix and solving the eigenvalue problem.
4. The phonon vector is obtained and stored in a separate file which is then used to put the distortion into the original file containing structural information.
5. The resulting structure is then submitted to a full relaxation process, keeping the cell volume fixed (changing volume may make the polar mode disappear).
6. If the relaxed structure does not possess the desired subgroup structure, redo step 4 using a different distortion amplitude.

[1] Department of Materials Science and Engineering, Northwestern University, Evanston, Illinois 60208, United States

After fully relaxing each subgroup phase, it is compared to the parent structure in terms of its *total distortion* and *energy gain*. The former is given by the square root of the sum of the square of all atomic displacements within a primitive unit cell of the reference structure and was determined via `AMPLIMODE`. The latter simply measures the difference of the total ground state energy of the distorted and the parent structure (a negative value implies that the low-symmetry structure is energetically favorable).

The procedure in this section was carried out with SCAN, PBEsol as well as LDA and excluding U.

Finally, the phonon-dispersion was calculated for the tetragonal FE P4mm phase using SCAN since this phase is expected to saturate the TO1 mode.

Chapter 3

Results

In this chapter I present the resulting phonon dispersions in cubic KTO under various computational approaches. The data is supplemented by electronic properties like band gaps and band structures. In the last Section, I discuss the tetragonal FE phase.

3.1 Lattice constant, band gap and band structures

The relaxed lattice constants for the tested functionals with different values of U are plotted in Fig. 3.1 (top). Starting with U=0 eV, LDA underestimates the experimental lattice constant by approximately 1% ($\sim$ 0.04Å). SCAN, PBEsol and HSE predict a value very close to the experimental one (3.984 Å [9]), overestimating it only by approximately 0.06, 0.10 and 0.20% respectively. Calculations using PBE are highly overestimating the lattice constant by about 1%. The plot also reveals that a_0 changes roughly as a linear function of U. The experimental value is most accurately predicted with either SCAN at zero U, or with LDA at approximately U=6 eV.

Figure 3.2 shows the electronic band structure for various functionals and U values. Electronic band structures are very similar for each functional. The electronic band gap is indirect and going from the Gamma point of the conduction to the R point of the valence band for all functionals. The value of the gap on the other hand differs greatly between the functionals, as seen from Fig. 3.1 (bottom). First of all, consider the case with zero U: The experimental value (3.64 eV [34]) is highly underestimated by all functionals besides HSE. The hybrid functional reproduces the band gap with a derivation of only around -5% ($\sim$ 0.5 eV). Besides the hybrid approach SCAN comes closest, underestimating the gap by about 30% ($\sim$ 1.1 eV). PBE, PBEsol and LDA are even worse with errors of more than 40% ($>$ 1.5 eV). Including SOC within the GGA functionals and SCAN leads to a decrease of the band gap by roughly 0.3 eV. By including U the band gap increases, as shown in the band structure plots of Fig. 3.2. SCAN+U=5.4 eV approximately reproduces the experimental value of the band gap. The dependence of the band gap on U is approximately linear, similar as the U dependence of the lattice constant. On the other hand PBE, PBEsol and LDA an unseemly-large value of U>8 would be needed to reproduce it.

Values of the relaxed lattice constants and band gaps in form of tables can be found in the Appendix (Tab. C.1 and C.2).

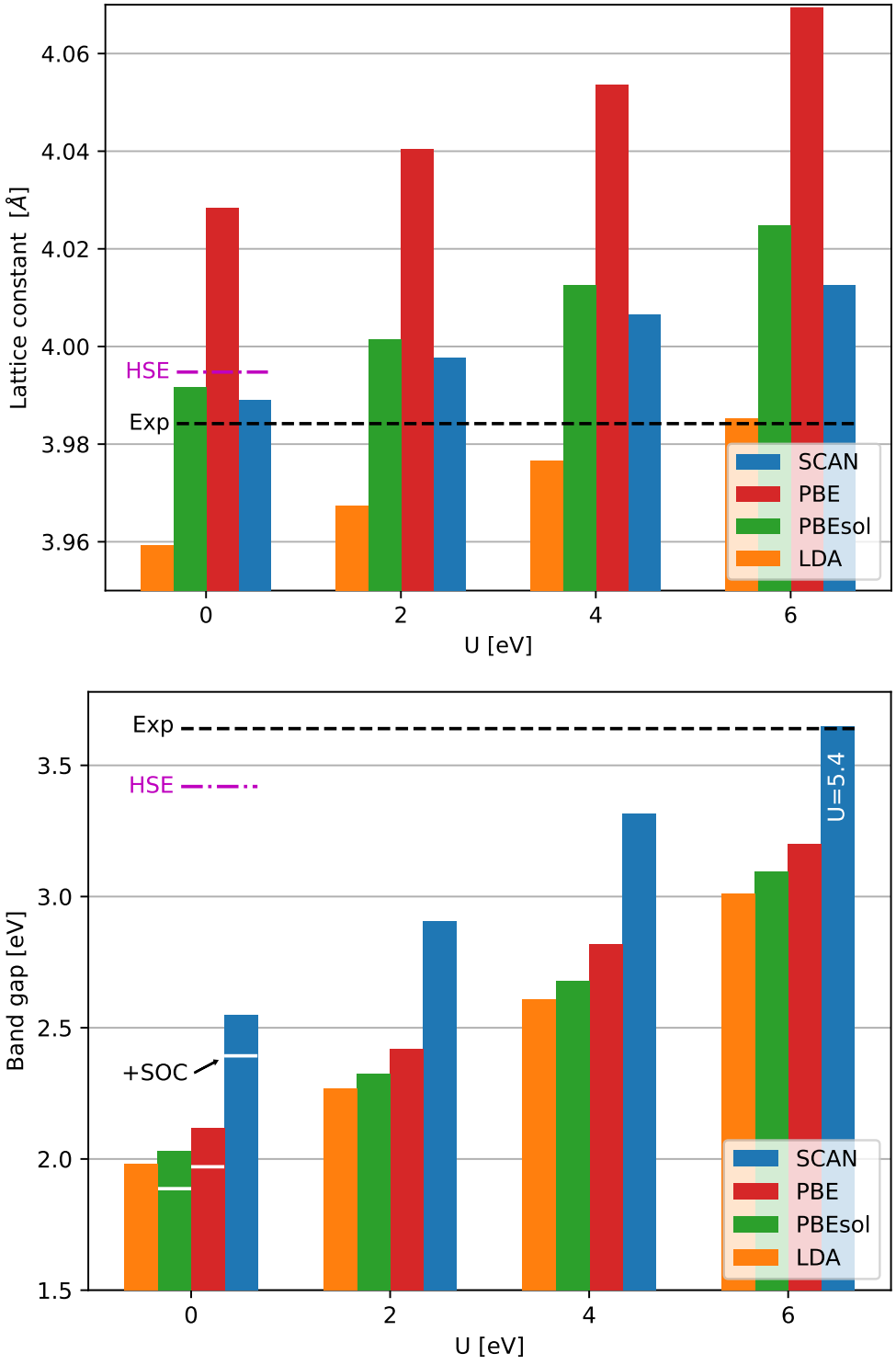

Figure 3.1: *Structural and electronic optimization:* The relaxed lattice constant (top) and the electronic band gap at the experimental lattice (bottom) for each functional, including different values of U. For SCAN, PBE and PBEsol at U = 0, spin orbit coupling was also introduced.

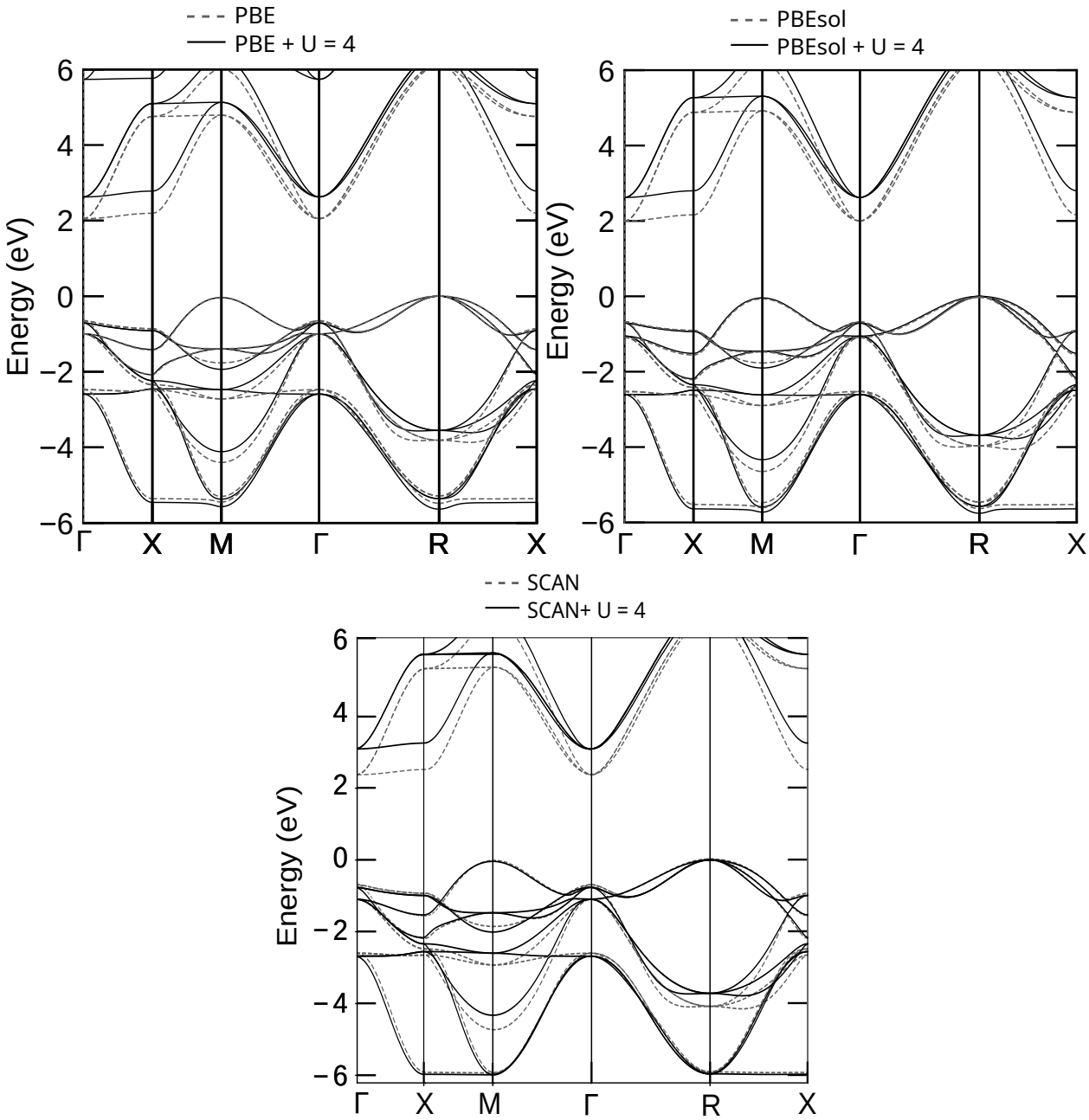

Figure 3.2: *Electronic band structure:* Band structures using the experimental lattice constant and the functionals PBE, PBEsol, SCAN. Each subplot compares the band structure without U and with U = 4. The band gap is between the Γ point of the conduction and the R point of the valence band. Including U decreases the band gap.

3.2 Phonons

3.2.1 Phonon dispersion using different functionals

The phonon dispersions for the different functionals are shown in Fig. 3.3 as obtained by using the relaxed lattice constant and with U=0 eV. In general PBEsol and LDA show a very similar dispersion relation with no imaginary modes. Conversely, using SCAN, the TO1 mode is imaginary. Moreover, also the other modes are different and in general have higher frequencies using SCAN. With a value of around 1.9 THz PBEsol is closest to the experimental value of the TO1 frequency of $\sim$ 0.7 THz (at 20K).

Pressure can control the instability of the TO1 phonon mode. To capture the TO1 mode at the transition point, its frequency is shown in Fig. 3.4 for the three functionals computed at different lattice constants. As the lattice constant is increased from the relaxed values, the mode gets imaginary between 3.96 and 3.98 Å for LDA and between 4.01 and 4.03 Å for PBEsol. Although the relaxed lattice constants of SCAN and PBEsol are similar, PBEsol predicts a stable mode for way larger lattice constants than SCAN.

3.2.2 SCAN+U and isotropic pressure

The comparison of the dispersions using the experimental versus the relaxed lattice constant is shown in Fig. 3.5. Since SCAN overestimates the experimental lattice constant only slightly, the difference of these two dispersions is small. There are imaginary modes at the Γ-, the X- as well as the M-point of the first Brillouin zone. More interestingly is the role of the U parameter. As the value of U is increased step by step (leaving the lattice unchanged), the modes exhibit a significant shift in frequency, as displayed in Fig. 3.6. The TO1 mode exhibits the most striking difference: in fact, at Γ it gains approximately 9 THz from U = 0 to 3 eV.

Phonon dispersions using SCAN+U=2 eV for different values of the lattice constant a_0 are shown in Fig. 3.7 . As a_0 is increased from its relaxed value the phonon modes soften in general. Comparing the different modes at the Γ point, the TO1 mode is strongly affected and becomes imaginary somewhere between 4.00 and 4.01 Å.

Fig. 3.8 captures the behaviour of the TO1 mode on the lattice constant and on U in a more qualitative way, as it shows for which values the mode is imaginary. The figure shows also additional information on the electronic band gap. It indicates that mode gets imaginary approximately on a line in the diagram. The electronic band gap increases for larger values of U, and increases for smaller values of a_0. Taking the setup without U as an example: From a_0 = 4.02 to 3.96 Å the band gap increases by around 5.7%.

Fig. 3.9 captures the frequency of the TO1 mode around the transition point for different values of U. Close to the transition, the frequency significantly drops, while further away the curve flattens out.

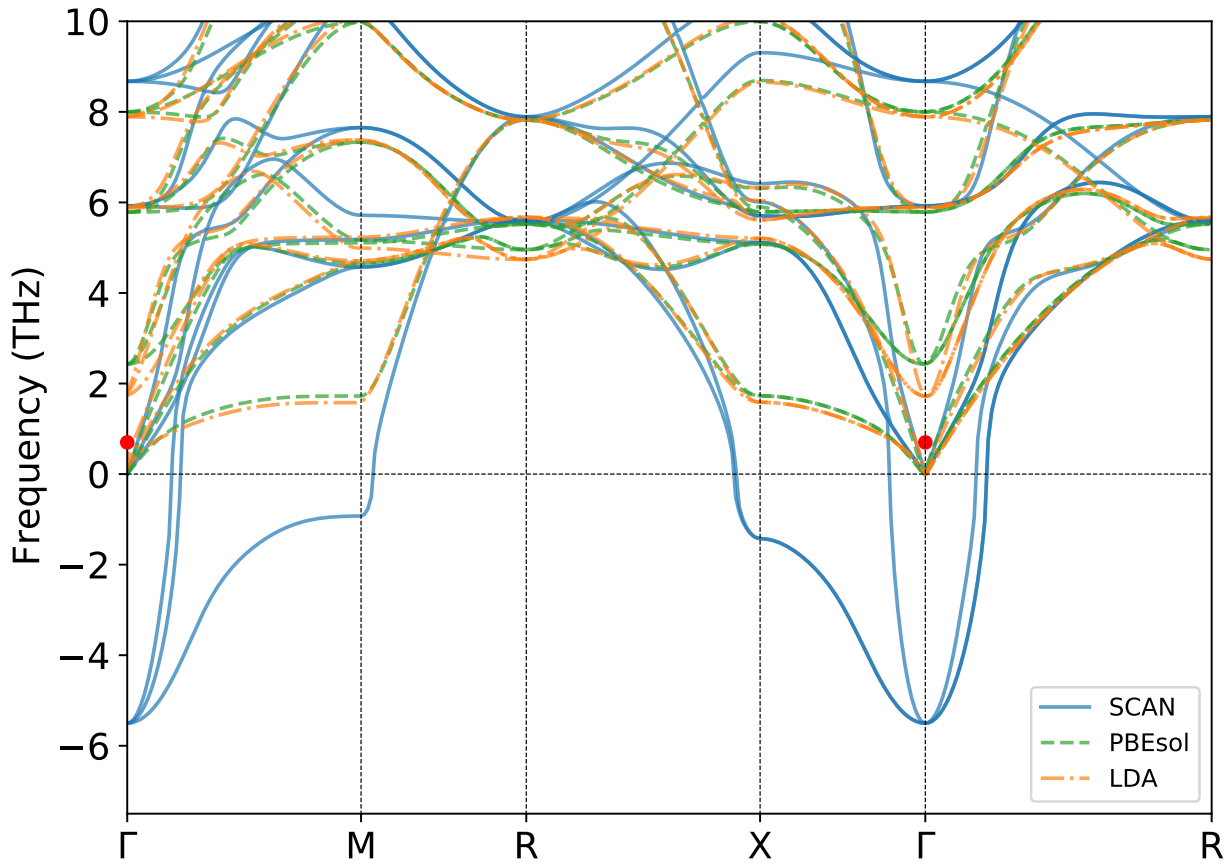

Figure 3.3: *Phonon dispersions with SCAN, PBEsol and LDA at their relaxed lattice constant (no U).* Experimental TO1 mode frequency is shown as a red dot.

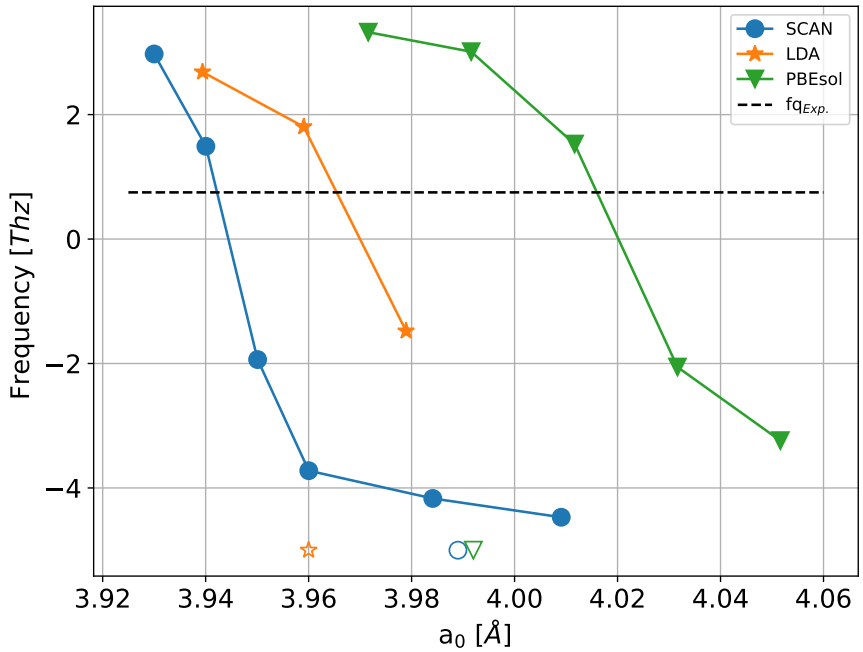

Figure 3.4: *Volume dependence of the TO1 mode in using SCAN, LDA and PBEsol without U.* Relaxed lattice constants for the three different functionals are indicated as non-filled symbols at the bottom (position with respect to y-axis to be ignored). The horizontal dashed line indicates the experimentally measured frequency ($\sim$ 0.7 THz).

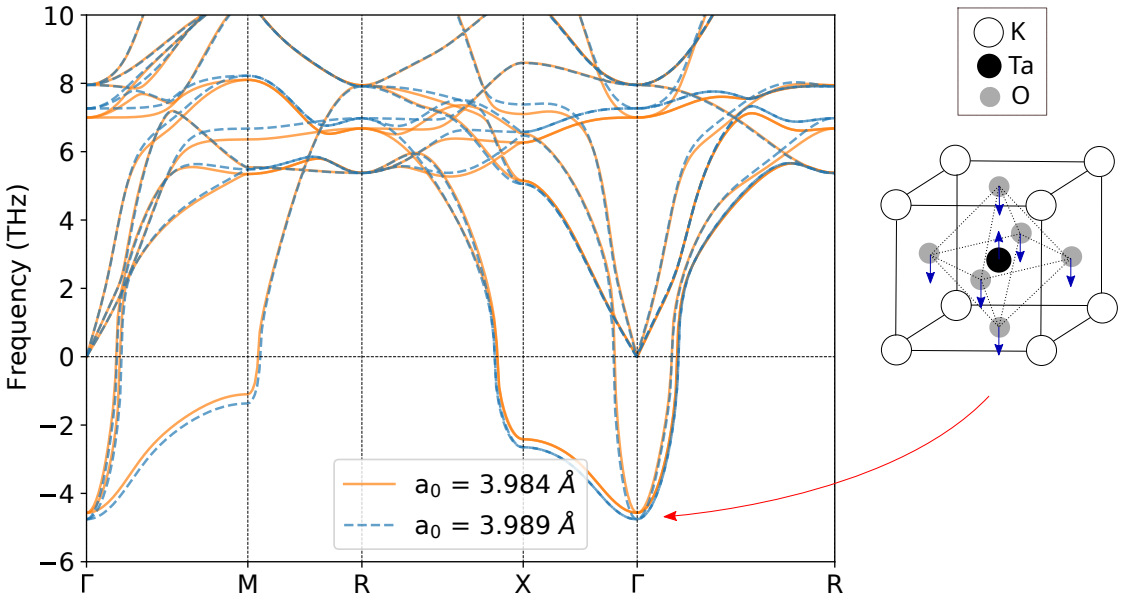

Figure 3.5: *Phonons with SCAN at experimental and relaxed lattice:* Imaginary frequencies are present at several locations for both setups. The imaginary TO1 mode corresponds to an opposite movement of the Ta and O atoms.

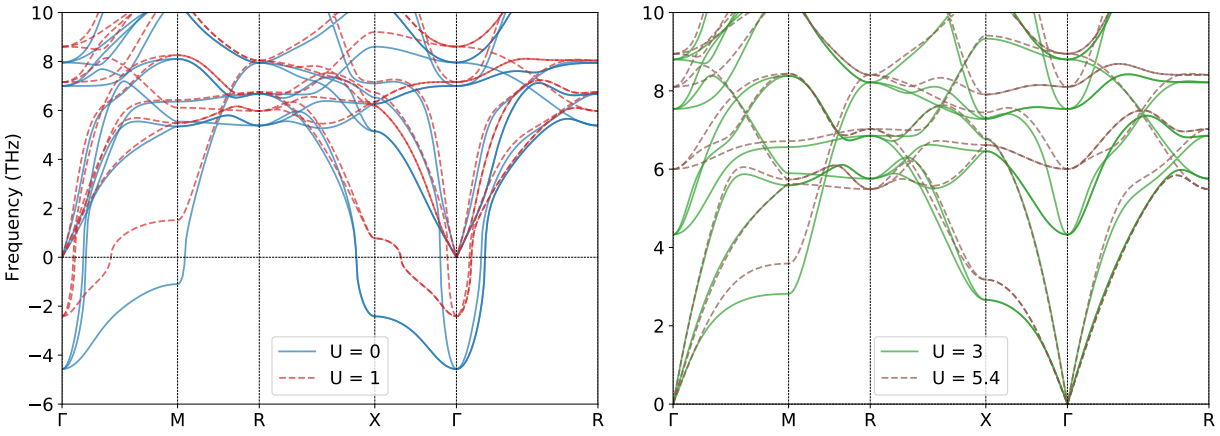

Figure 3.6: *U-dependence of phonons in experimental KTO using SCAN:* As U is increased, the TO1 mode is stabilized.

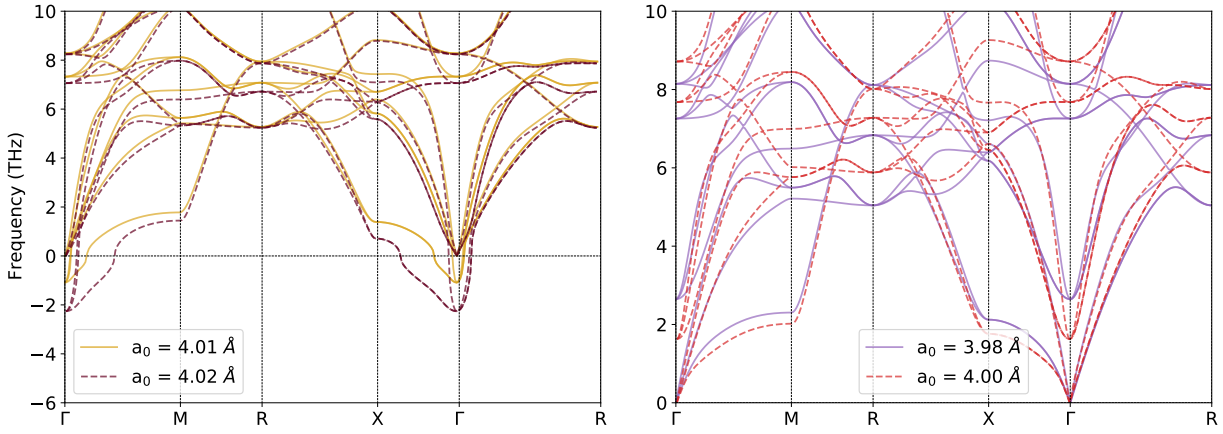

Figure 3.7: *Volume dependence of phonons in KTO using SCAN+U=2:* As cell volume is increased, starting with the experimental lattice constant, the TO1 mode gets imaginary.

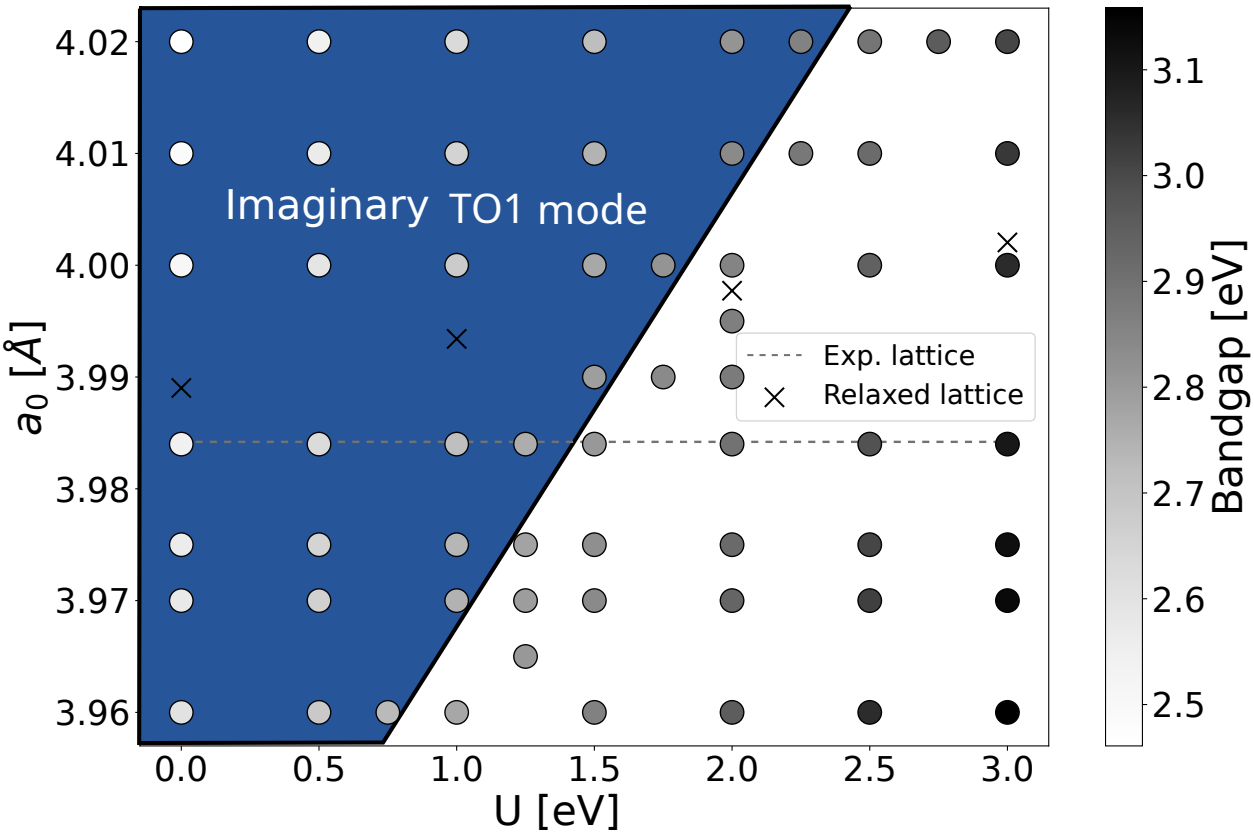

Figure 3.8: *TO1 mode and band gap using SCAN:* The value of the lattice constant is shown on the vertical axis and the value of U on the horizontal axis. Each data point corresponds to one phonon calculation as well as one computation of the band gap. The blue area indicates the data for which the TO1 mode is imaginary. Furthermore the experimental lattice constant and the relaxed lattice constant are marked.

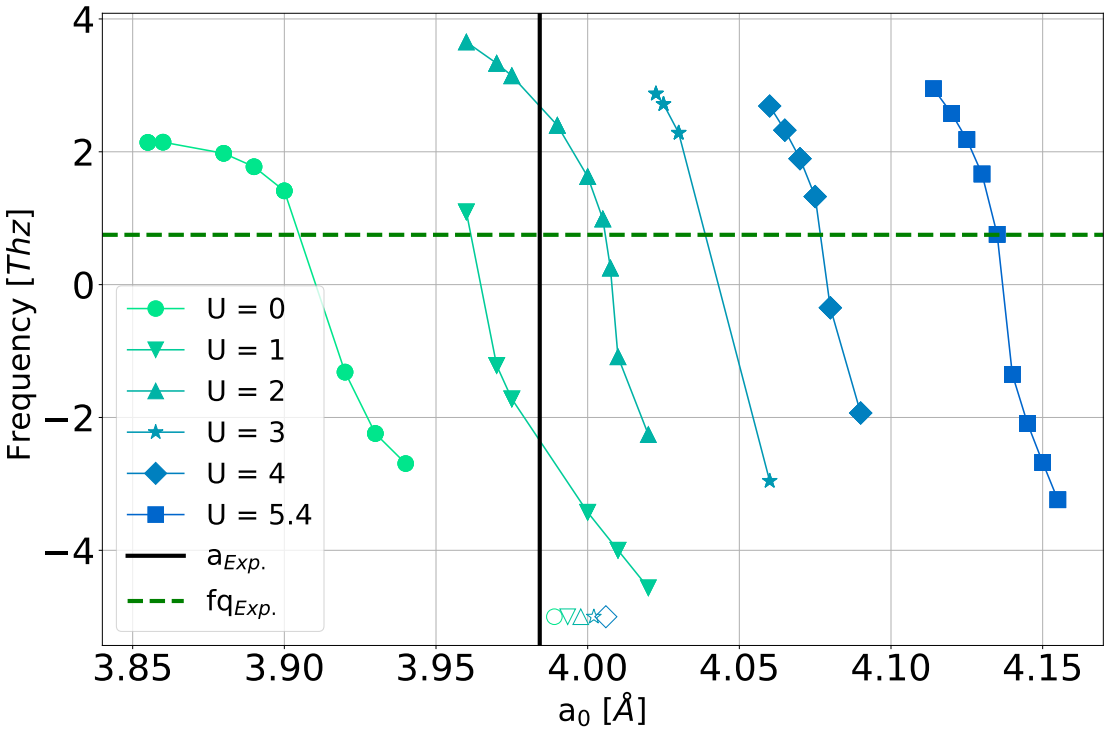

Figure 3.9: *TO1 soft mode using SCAN:* Frequency of TO1 around the transition point plotted against the size of the unit cell, for different values of U. Relaxed lattice constants for U=0,1,2 and 3 eV are indicated as non-filled symbols at the bottom in the middle of the plot (position with respect to y-axis to be ignored). Experimental frequency of TO1 and experimental lattice constant are shown as a horizontal dashed and a vertical line, respectively.

3.3 A ferroelectric ground state using SCAN

After full relaxation, all polar low symmetry phases show only a small total distortion from the cubic phase. As Fig. 3.10a shows, the total distortion is smaller than 0.10 Å for all functionals. For PBEsol the distortion is even lower than 0.01 Å. Also there is no low symmetry structure which has a striking difference compared to the others. What follows is only a small energy gain of values less than 10^{-2} eV for all subgroups as well as functionals (Fig. 3.10b). Despite the small values, SCAN is the only functional predicting an energy gain for all subgroups, which means that all the low symmetry phases associated with the TO1 mode are energetically more favourable than the cubic structure.

The dispersion in the tetragonal P4mm phase using SCAN is shown in Fig. 3.11a. The TO1 mode which is imaginary in the cubic phase is now stabilized in the fully relaxed ferroelectric structure P4mm.

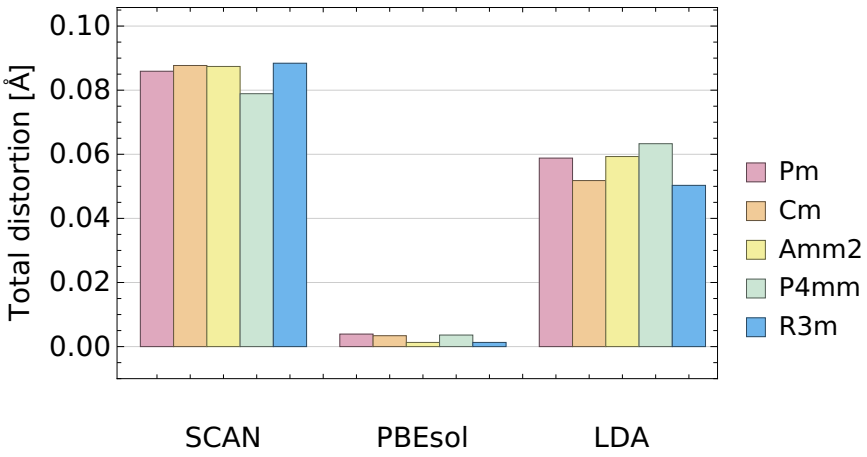

(a) *Total distortion:* The square root of the sum of the square of all atomic displacements within a unit cell of the reference structure. The phases are distinguished using different colors. Zero U was used.

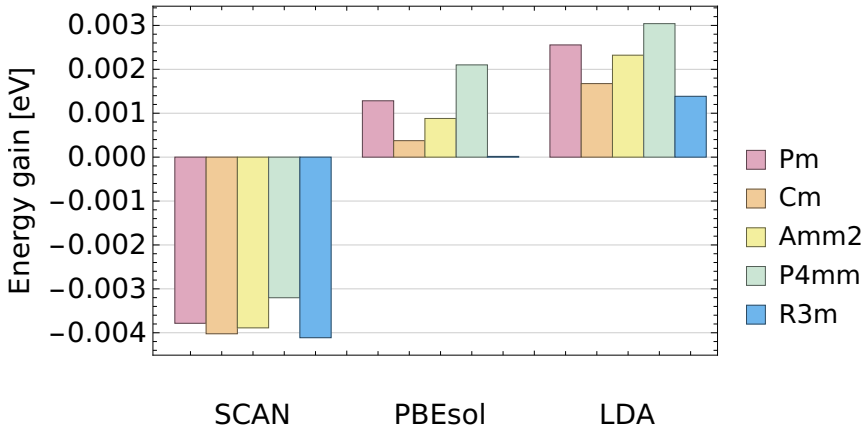

(b) *Energy gain:* Difference of the total ground state energy between the unit cell of distorted and the parent structure, respectively. Negative values indicate energetically more favourable phases. The phases are distinguished using different colors.

Figure 3.10

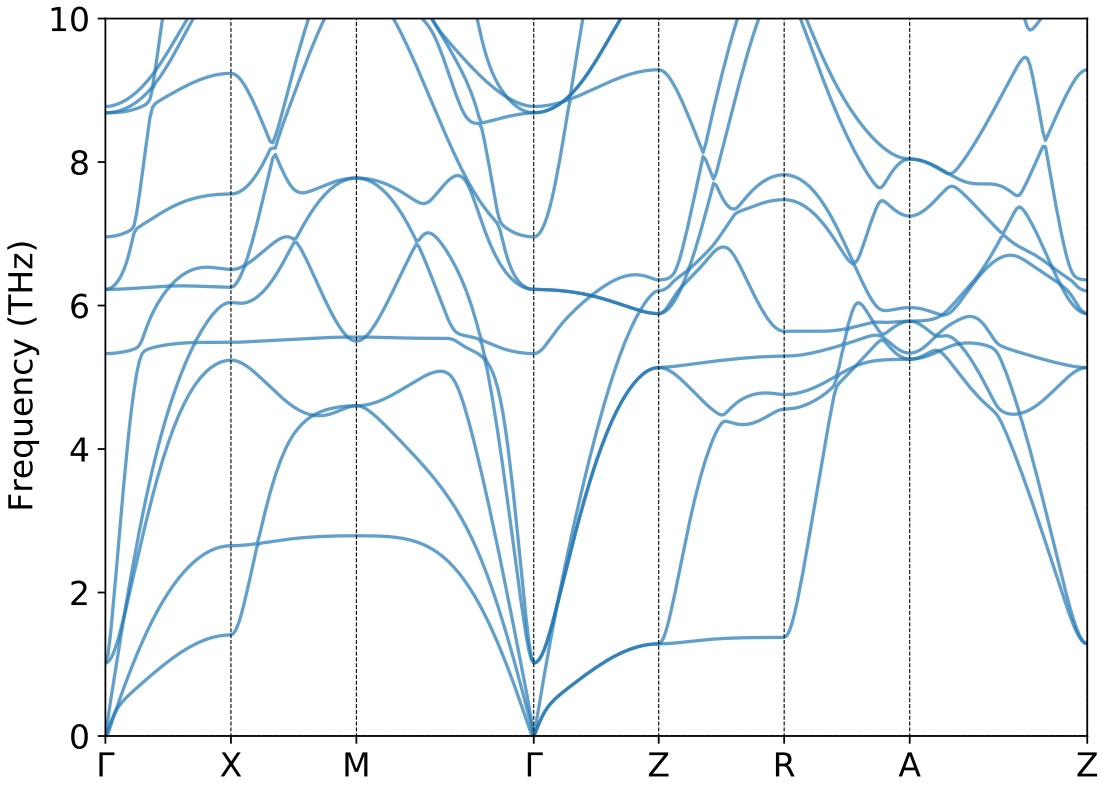

(a) *Phonons of the ferroelectric P4mm phase with SCAN and zero U.*

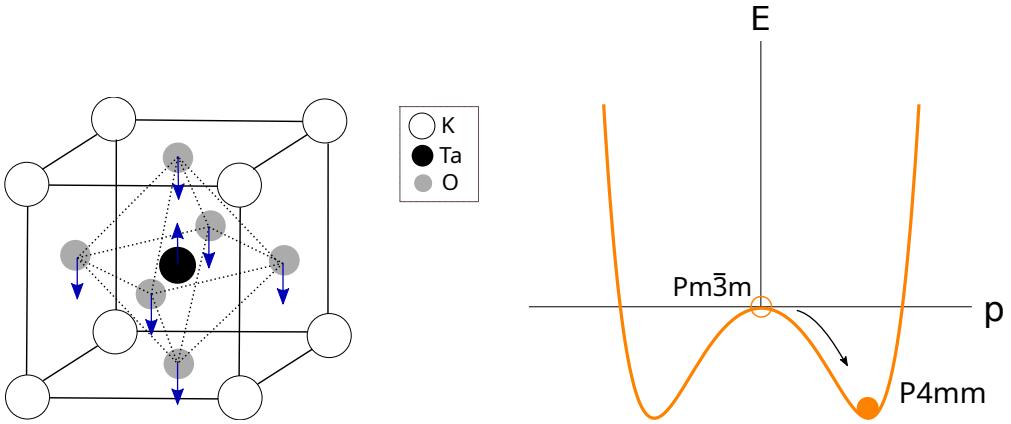

(b) *Ferroelectric distortion:* The ferroelectric tetragonal P4mm phase results from an opposite shift of Ta and O atoms. The ground state energy is lower than the non-ferroelectric cubic structure.

Figure 3.11

Chapter 4

Discussion

4.1 Band gap and relaxed lattice constant

I have shown that SCAN and PBEsol give a significant improvement over PBE and LDA in predicting the equilibrium properties of cubic KTO. HSE shows a similar good performance but has the disadvantage of high computational cost. As expected, the lattice constant is underestimated by LDA, as atoms tends to "overbind". On the other hand, PBE tends to "overcorrect" the cell volume. Overall, the estimated lattice constants are in good agreement with similar DFT studies (see Table C.1).

For the electronic calculations it is inevitable to introduce an U to accurately account for the band gap. The results reveal an indirect gap between the R- and the $\Gamma-$ point of the first Brillouin zone, which agrees with experiment. As expected from DFT the value is underestimated by all functionals, on the other hand the hybrid functional HSE achieves a value close to experiment. Including SOC only slightly decreases the band gap due to band splitting. On the other hand, the U parameter induces a great change in the band gap. SCAN has the overall best performance and predicts the experimental band gap at about U=5.4 eV. This prediction is not fully satisfied by cRPA calculations that suggest a value of $U > 3.25$ but at most 4 eV (see Supplementary Information of [21]).

4.2 Quantum paraelectric or ferroelectric?

The phonon dispersions for cubic KTO using SCAN were studied in great detail by changing the unit cell size as well as the U parameter. Imaginary phonons were found, and the most striking one was identified as the ferroelectric Γ_4^- (TO1) mode, corresponding to an opposite movement of the oxygen octahedron and the tantalum atom. The softening of this mode by increasing the lattice cell supports experimental measurements which show a drastic decrease in frequency by lowering the temperature (see [35]). This is because as temperature rises, the distances between atoms increase and thus the restoring force of the FE mode decreases, leading to a frequency decrease. The lattice constant at which the frequency of the TO1 mode gets imaginary (a_T) using a specific U, is compared with the relaxed lattice constant (a_R) at that U value by taking the relative difference. The result is plotted in Fig. 4.1.

In a recent DFT study on KTO and STO, a strong effects of the lattice parameter on the shape of the double-well potential is reported. They describe KTO as a weak quantum paraelectric but conclude that KTO may transform to a ferroelectric state as the cell volume increases (see [36]), underpinning the results of this work. Again using SCAN, the mode was finally stabilized and a ferroelectric tetragonal ground state of KTO was found. In terms of atomic distances, the relaxed tetragonal structure differs only slightly from the cubic one,

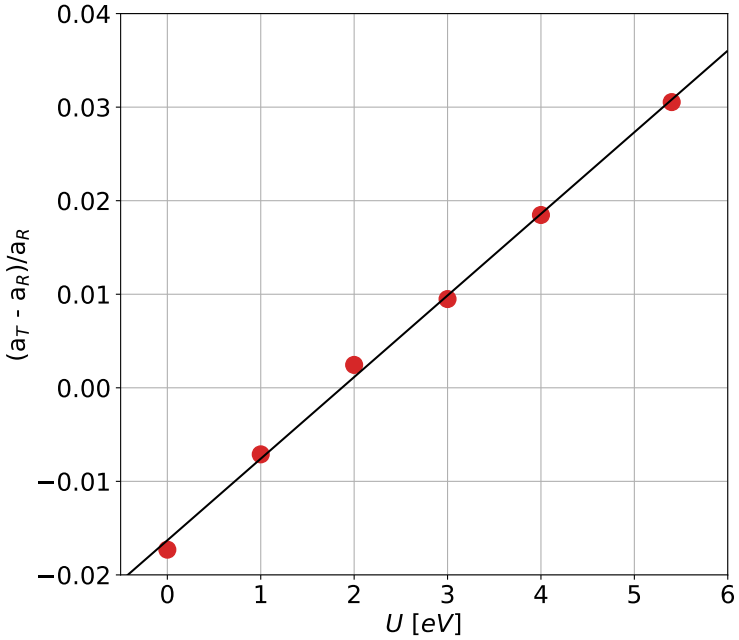

Figure 4.1: The lattice constant a_T, where the frequency of the TO1 mode is compared to the relaxed lattice constant a_R for different values of U. A linear fit is added.

indicating a very weak ferroelectricity. Also, in contrast to SCAN, the functionals PBEsol and LDA do not show any imaginary modes at their relaxed lattice parameters. These results together indicate a quantum paraelectric behavior.

Experimental measurements of the phonons predict a TO1 frequency of around 0.75 THz at 20K. By carefully looking at Fig. 3.9, we can see that the only value for which SCAN is close to the experimentally obtained TO1 frequency at a relaxed lattice constant, is for (a, U) = (3.988, 2). Fig. 4.2 shows the dispersions for (a, U) = (4.00, 2) and (3.975, 1.25) with experimental values included. From the right plot we see that the experimental TO1 values as well as the values from Γ to X are well reproduced.

Taking a look at Fig. 3.11a, we see that the modes which were imaginary in the cubic phase are condensed, the TO1 mode at Γ lies close to the experimental one of ~ 0.7 THz. However the agreement with experiment is not good at other points and therefore a FE phase has to be excluded. More studies including U in the FE phase are required to see whether the experimental frequencies are reproduced better.

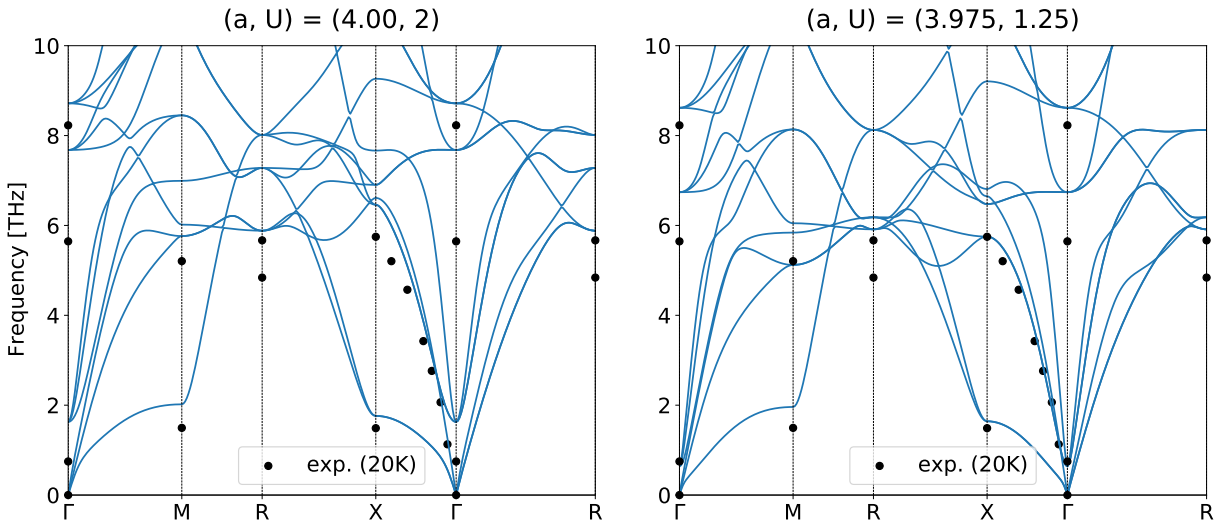

Figure 4.2: *Phonon dispersions of the cubic phase using SCAN+U.* Experimental values at 20 K are included.

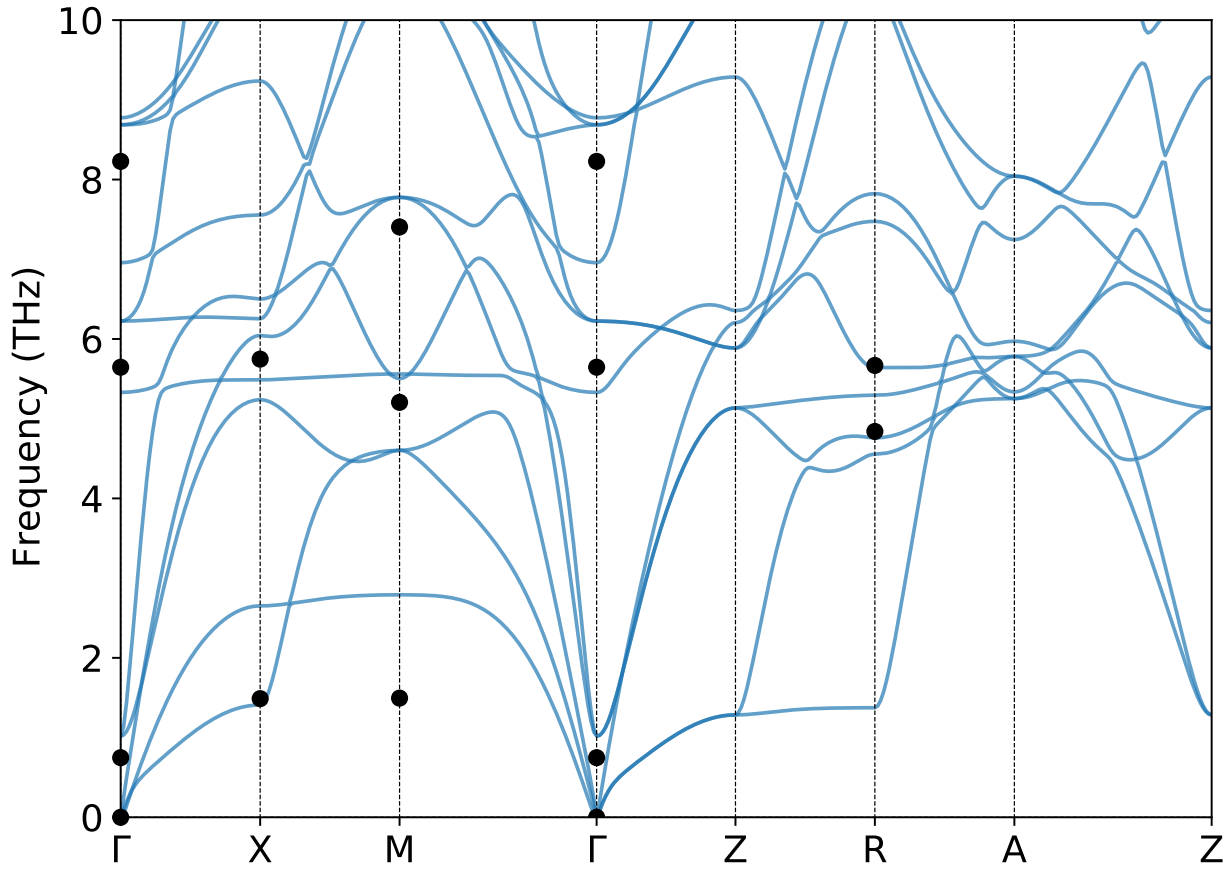

Figure 4.3: *Phonons of the ferroelectric P4mm phase with SCAN and zero U.* Experimental values at 20 K are shown as black dots.

Chapter 5

Conclusion and Outlook

KTO remains a controversial material in terms of its ferroelectric properties. On the one hand experimental results suggest that the ground state is paraelectric within the entire temperature range - on the other hand the behavior of the dielectric constant at low temperatures is anomalous [8]. This work supports the quantum paraelectric nature of KTO, where the material is about to be ferroelectric, but the transition ultimately is prevented by quantum fluctuations.

More insights into polarization in bulk KTO could be gained by continuing the structural search in this work with including distortions corresponding to imaginary phonon modes at other points of the Brillouin zone. It remains to be discovered if the lower symmetry structure is polar and has a lower ground state energy than the cubic one. Furthermore, including anharmonic effect in the phonon calculations may reveal an improved understanding of the ferroelectric properties.

Appendix

As a part of the present work is based on a symmetry analysis of KTO, I will give a short introduction on the mathematical background of representation theory and show by example how it can be used to decompose the vibrational modes of KTO at Γ into irreducible representations.

A Group theory and group representations

In the following section, some basic definitions of group theory and the most essential results of representation theory are given. The proofs can be found in [37].

Definition A.1. A *group* G is a collection of objects $a, b, c, ...$ including an operation, denoted by $*$ and satisfying the following axioms:

1. $a * b \in G$ (closure)
2. $a * (b * c) = (a * b) * c$ (associative)
3. there exists an identity element, e, such that $a * e = a$ for all $a \in G$.
4. for every a, there exists an inverse element, a^{-1}, such that $a * a^{-1} = e$.

The number of elements in the group is called the *order* of the group.

Definition A.2. A *subgroup* H of G are the set of elements H which is contained in G and for which the following is true:

i) the product of any pair of elements in H is in H,

ii) if $a \in H$, then $a^{-1} \in H$.

The existence of an inverse implies that the identity element e is also included and because all elements in H are also in G they also obey the associative law.

Definition A.3. An element $a \in G$ is *conjugate* to an element $b \in G$ if there exists another element $x \in G$ such that

$$a = xbx^{-1}.$$

Definition A.4. All elements of a group which are conjugate to each other form an *equivalence class*, also simply called a *class*.

Definition A.5. A mapping from one group G to another group G' which preserve group products but is no necessarily one to one is called a *homomorphism*.

Definition A.6. A *representation* of a group G including elements U_1, U_2, ... is a homomorphic mapping of G onto a collection of finite-dimensional matrices, denoted as $D(U_1)$, $D(U_2)$, $D(U_3)$, ...

Definition A.7. If a representation $D(U_i)$ can be brought into the form (block diagonal)

$$\overline{D}(U_i) \equiv SD(U_i)S^{-1} = \begin{bmatrix} D^{(1)}(U_i) & & & 0 \\ & D^{(2)}(U_i) & & \\ & & \ddots & \\ 0 & & & D^{(k)}(U_i) \end{bmatrix}, \qquad (*)$$

where S is a matrix which is the same for all U_i, then it is considered to be a sum of representations, called a *reducible representation.*

Definition A.8. A representation which cannot be reduced in this manner is called a *irreducible representation (IR)* .

Definition A.9. The trace of $D(U)$ is called the *character* of U in the representation $D(U)$ and is denoted by $\chi(U)$.

The remarkable discoveries of representation theory may be summarized by the following equations:

$$\begin{aligned} \sum_{\nu=1}^{N} n_\nu^2 &= g \\ k &= N \\ \sum_{U\in G} \sqrt{\frac{n_\mu}{g}} D_{lk}^{(\mu)*}(U) \sqrt{\frac{n_\nu}{g}} D_{ij}^{(\nu)}(U) &= \delta_{jk}\delta_{il}\delta_{\mu\nu} \\ \sum_{\nu=1}^{N}\sum_{i=1}^{n_\nu}\sum_{j=1}^{n_\nu} \sqrt{\frac{n_\nu}{g}} D_{ij}^{(\nu)}(U) \sqrt{\frac{n_\nu}{g}} D_{ij}^{(\nu)*}(U') &= \delta_{UU'} \\ \sum_{i=1}^{k} \sqrt{\frac{g_i}{g}} \chi_i^{(\mu)*} \sqrt{\frac{g_i}{g}} \chi_i^{(\nu)} &= \delta_{\mu\nu} \\ \sum_{\nu=1}^{k} \sqrt{\frac{g_i}{g}} \chi_i^{(\nu)} \sqrt{\frac{g_j}{g}} \chi_j^{(\nu)*} &= \delta_{ij} \end{aligned} \qquad (**)$$

Here g defines the order of the group, g_i is the number of elements in the i-th class, k the number of classes, N the number of IRs and n_ν the dimension of the ν-th IR.

Representation theory has important applications in crystallography and solid-state physics. It allows to identify the normal modes of crystals and molecules by considering only symmetry operations on the system. To achieve this, an important relationship is derived in the following. If a given representation D is written in block-diagonal form (see *), then the character χ_i of a given class is

$$\chi_i = a^{(1)}\chi_i^{(1)} + a^{(2)}\chi_i^{(2)} + ... + a^{(N)}\chi_i^{(N)} \equiv \sum_{\nu=1}^{N} a^{(\nu)}\chi_i^{(\nu)},$$

since the characters are the traces of the representative matrices. $a^{(v)}$ defines the number how often the irreducible representation occurs in the decomposition of D. Multiplying this

equation on both sides by $g_i\chi_i^{(\mu)*}$, summing over i and using the orthogonality relation for characters (see **??**) we get

$$a^{(\mu)} = \frac{1}{g}\sum_{i=1}^{k} g_i\chi_i^{(\mu)*}\chi_i. \qquad (***)$$

Thus the number of times a given irreducible representation occurs in an arbitrary representation is determined from the characters of that representation. Sometimes this equation is referred to as the *magic counting formula* and is used to determine the vibrational normal modes of molecules and crystals.

In the following section we make use of representation theory to determine the vibrational modes of KTO at the Γ point in terms of IRs of the point group.

B Symmetry of KTO at Γ: Decomposition into IRs.

As the normal modes of a crystal are represented as waves, we obtain the irreducible representations of the space group of the crystal from the IRs of the point group which leave the wave vector $\mathbf{k}$ unchanged. As for KTO the point group of symmetry at Γ ($\mathbf{k} = 0$) is O_h.

With the magic counting formula (see ***), we obtain the decomposition into irreducible representations: g_i is the number of elements for each class i; g the order of the point group; $\chi_i^{(\mu)*}$ the character for i and the IRs Γ_μ; $\chi_i = w_i(2\cos\phi \pm 1)$ with w_i the numbers of atoms which are invariant under the operation i.

g_i, w_i and then χ_i are calculated by studying the symmetry operations, illustrated in Figure B.1. There are three C_4, three C_2, four C_3 and six $C_{2'}$ axes, as well as three horizontal mirror planes σ_h, six dihedral mirror planes σ_h and an inversion center I. The rotation-reflection axes S_4 and S_6 are the same as C_4 and C_3 respectively and are therefore not shown. The axis (for clarity not all) of the symmetry operations are indicated. For each class, the remaining data is included in table B.1.

Applying the magic counting formula we get the decomposition

$$\Gamma_{vibr.} = 4\Gamma_4^- + \Gamma_5^-.$$

Since KTO has five atoms within the unit cell and 12 degrees of freedom there are three triply degenerate phonon modes with the IR Γ_4^- and one triply degenerate phonon mode with IR Γ_5^-.

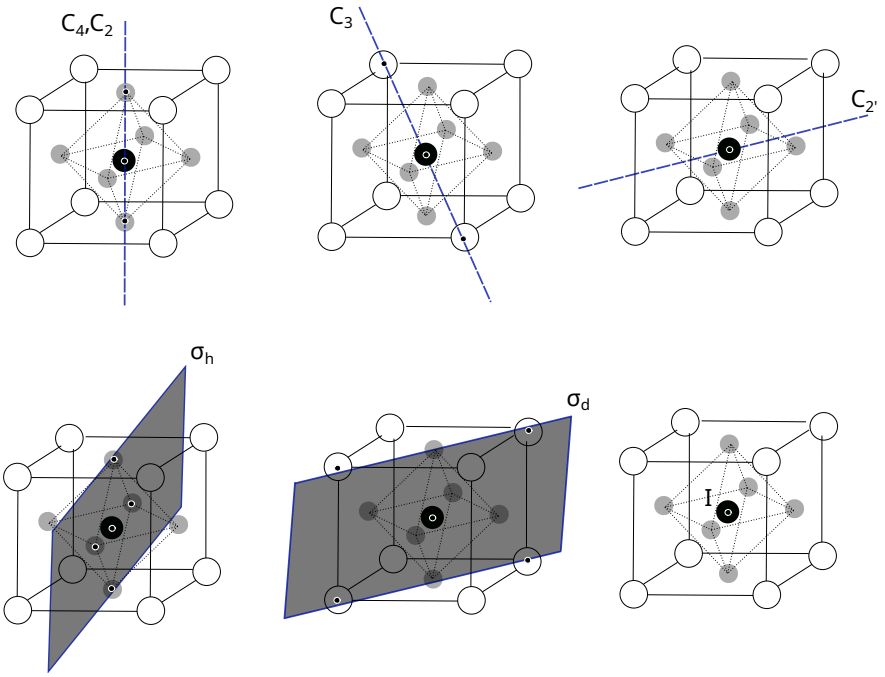

Figure B.1: Symmetry elements of the point group O_h to which KTO belongs at Γ (S_4 and S_6 omitted). For clarity reasons only one symmetry axis is indicated in each drawing.

O_h	E	C_4	C_2	C_3	$C_{2'}$	I	S_4	S_6	σ_h	σ_d
Γ_1^+ (A_{1g})	1	1	1	1	1	1	1	1	1	1
Γ_2^+ (A_{2g})	1	-1	1	1	-1	1	-1	1	1	-1
Γ_3^+ (E_g)	2	0	2	-1	0	2	0	2	-1	0
Γ_4^+ (T_{1g})	3	1	-1	0	-1	3	1	-1	0	-1
Γ_5^+ (T_{2g})	3	-1	-1	0	1	3	-1	-1	0	1
Γ_1^- (A_{1u})	1	1	1	1	1	-1	-1	-1	-1	-1
Γ_2^- (A_{2u})	1	-1	1	1	-1	-1	1	-1	-1	1
Γ_3^- (E_u)	2	0	2	-1	0	-2	0	-2	1	0
Γ_4^- (T_{1u}) (T_{15})	3	1	-1	0	-1	-3	-1	1	0	1
Γ_5^- (T_{2u}) (T_{25})	3	-1	-1	0	1	-3	1	1	0	-1
g_i	1	6	3	8	6	1	6	8	3	6
χ_i	15	3	-5	0	-3	-15	-3	0	5	3

Table B.1: Character table of point group O_h. The irreducible representations are given in the *Miller-Love notation* [38] $\Gamma_x^{\pm}$ as well as in the Mulliken notation [39] in brackets. For the IR Γ_4^- and Γ_5^- another common notation in solid state physics is given [40]. Furthermore the number of elements per class g_i and the character of the crystal χ_i are supplied.

C Structural and electronic optimization

The following two tables contain the data of Fig. 3.1.

U	SCAN	PBE	PBEsol	LDA	HSE
0	3.989	4.028	3.992	3.960	3.995
0 Ref.	3.982[a]	4.028[a]	3.989[b]	3.959[a]	3.997[c]
1	3.993				
2	3.998	4.040	4.002	3.967	
3	4.002				
4	4.006	4.054	4.013	3.977	
5	4.011				
5.4	4.012				
6	4.015	4.070	4.025	3.985	
Experimental: 3.984					

a. Ref. [41]
b. Ref. [42]
c. Ref. [43]

Table C.1: *Structural optimization:* The relaxed lattice constant (in Å) for each functional, including different values of U (in eV). The references given do not use any U.

U	SCAN		PBE		PBEsol		LDA	HSE Rel.
	Exp.	Rel.	Exp.	Rel.	Exp.	Rel.	Rel.	Rel.
0	2.55	2.53	2.12	2.12	2.03	2.02	1.98	3.42
0+SOC	2.39	1.93	1.89					
1	2.72	2.69						
2	2.90	2.86	2.42	2.31	2.33	2.22	2.27	
3	3.10	3.05						
4	3.32	3.26	2.82	2.62	2.68	2.53	2.61	
5	3.55	3.47						
5.4	3.65	3.56						
6			3.20	2.97	3.09	2.87	3.01	
8			3.70	3.32	3.59	3.22	3.48	
Experimental: 3.64								

Table C.2: *Electronic band gap:* The indirect Γ-R band gap (in eV) of cubic KTO for different values of U (in eV) and functionals. For SCAN, PBE and PBEsol at U = 0, spin orbit coupling was also introduced.

Bibliography

[1] L. Landau and E. Lifshitz, *Statistical Physics: Volume 5*, Bd. 5 (Elsevier Science, 2013).

[2] H. Uwe and T. Sakudo, Phys. Rev. B **13**, 271 (1976).

[3] G. Grosso and G. P. Parravicini, "Ix - lattice dynamics of crystals," in *Solid State Physics* (Academic Press, London, 2000) pp. 307–348.

[4] R. H. Lyddane, R. G. Sachs, and E. Teller, Phys. Rev. **59**, 673 (1941).

[5] W. Cochran, Phys. Rev. Lett. **3**, 412 (1959).

[6] H. T. Stokes, D. M. Hatch, and J. D. Wells, Phys. Rev. B **43**, 11010 (1991).

[7] R. Wahl, D. Vogtenhuber, and G. Kresse, Phys. Rev. B **78**, 104116 (2008).

[8] J. K. Hulm, B. T. Matthias, and E. A. Long, Phys. Rev. **79**, 885 (1950).

[9] G. A. Samara and B. Morosin, Phys. Rev. B **8**, 1256 (1973).

[10] G. Shirane, R. Nathans, and V. J. Minkiewicz, Phys. Rev. **157**, 396 (1967).

[11] P. Hohenberg and W. Kohn, Phys. Rev. **136**, B864 (1964).

[12] W. Kohn and L. J. Sham, Phys. Rev. **140**, A1133 (1965).

[13] F. Tran, J. Stelzl, and P. Blaha, The Journal of Chemical Physics **144**, 204120 (2016).

[14] J. P. Perdew, K. Burke, and M. Ernzerhof, Phys. Rev. Lett. **77**, 3865 (1996).

[15] R. Van Noorden, B. Maher, and R. Nuzzo, Nature **514**, 550 (2014).

[16] J. P. Perdew, A. Ruzsinszky, G. I. Csonka, O. A. Vydrov, G. E. Scuseria, L. A. Constantin, X. Zhou, and K. Burke, Phys. Rev. Lett. **100**, 136406 (2008).

[17] P. Haas, F. Tran, and P. Blaha, Phys. Rev. B **79**, 085104 (2009).

[18] G. I. Csonka, J. P. Perdew, A. Ruzsinszky, P. H. T. Philipsen, S. Lebègue, J. Paier, O. A. Vydrov, and J. G. Ángyán, Phys. Rev. B **79**, 155107 (2009).

[19] J. Sun, R. C. Remsing, Y. Zhang, Z. Sun, A. Ruzsinszky, H. Peng, Z. Yang, A. Paul, U. Waghmare, X. Wu, M. L. Klein, and J. P. Perdew, Nature Chemistry **8**, 831 (2016).

[20] G.-X. Zhang, A. Reilly, A. Tkatchenko, and M. Scheffler, New Journal of Physics **20** (2018), 10.1088/1367-2630/aac7f0.

[21] M. Reticcioli, U. Diebold, G. Kresse, and C. Franchini, "Small polarons in transition metal oxides," in *Handbook of Materials Modeling: Applications: Current and Emerging Materials*, edited by W. Andreoni and S. Yip (Springer International Publishing, Cham, 2019) pp. 1–39.

[22] S. L. Dudarev, G. A. Botton, S. Y. Savrasov, C. J. Humphreys, and A. P. Sutton, Phys. Rev. B **57**, 1505 (1998).

[23] G. Kresse and J. Hafner, Phys. Rev. B **47**, 558 (1993).

[24] G. Kresse and J. Hafner, Phys. Rev. B **49**, 14251 (1994).

[25] G. Kresse and J. Furthmüller, Computational Materials Science **6**, 15 (1996).

[26] G. Kresse and J. Furthmüller, Phys. Rev. B **54**, 11169 (1996).

[27] A. Togo and I. Tanaka, Scripta Materialia **108**, 1 (2015).

[28] H. T. Stokes, S. van Orden, and B. J. Campbell, Journal of Applied Crystallography **49**, 1849 (2016).

[29] D. Orobengoa, C. Capillas, M. I. Aroyo, and J. M. Perez-Mato, Journal of Applied Crystallography **42**, 820 (2009).

[30] J. M. Perez-Mato, D. Orobengoa, and M. I. Aroyo, Acta Crystallographica Section A **66**, 558 (2010).

[31] A. M. Ganose, A. J. Jackson, and D. O. Scanlon, Journal of Open Source Software **3**, 717 (2018).

[32] A. V. Krukau, O. A. Vydrov, A. F. Izmaylov, and G. E. Scuseria, The Journal of Chemical Physics **125**, 224106 (2006).

[33] F. Birch, Phys. Rev. **71**, 809 (1947).

[34] G. E. Jellison, I. Paulauskas, L. A. Boatner, and D. J. Singh, Phys. Rev. B **74**, 155130 (2006).

[35] C. H. Perry, R. Currat, H. Buhay, R. M. Migoni, W. G. Stirling, and J. D. Axe, Phys. Rev. B **39**, 8666 (1989).

[36] T. Esswein and N. A. Spaldin, Phys. Rev. Research **4**, 033020 (2022).

[37] F. Byron and F. W., *Mathematics of Classical and Quantum Physics* (Dover Books of Physics, 1992).

[38] S. Miller and W. Love, *Tables of Irreducible Representations of Space Groups and Co-Representations of Magnetic Space Groups.* (Pruett Press, 1967).

[39] R. S. Mulliken, The Journal of Chemical Physics **23**, 1997 (1955).

[40] L. P. Bouckaert, R. Smoluchowski, and E. Wigner, Phys. Rev. **50**, 58 (1936).

[41] Y. Zhang, J. Sun, J. P. Perdew, and X. Wu, Phys. Rev. B **96**, 035143 (2017).

[42] H. Bouafia, S. Hiadsi, B. Abidri, A. Akriche, L. Ghalouci, and B. Sahli, Computational Materials Science **75**, 1 (2013).

[43] A. C. Garcia-Castro, P. Ghosez, E. Bousquet, and A. H. Romero, Phys. Rev. B **102**, 235140 (2020).